# Measurements of the $B \to X_s\gamma$ branching fraction and photon spectrum from a sum of exclusive final states

B. Aubert,[1] R. Barate,[1] D. Boutigny,[1] F. Couderc,[1] Y. Karyotakis,[1] J. P. Lees,[1] V. Poireau,[1] V. Tisserand,[1] A. Zghiche,[1] E. Grauges,[2] A. Palano,[3] M. Pappagallo,[3] A. Pompili,[3] J. C. Chen,[4] N. D. Qi,[4] G. Rong,[4] P. Wang,[4] Y. S. Zhu,[4] G. Eigen,[5] I. Ofte,[5] B. Stugu,[5] G. S. Abrams,[6] M. Battaglia,[6] A. B. Breon,[6] D. N. Brown,[6] J. Button-Shafer,[6] R. N. Cahn,[6] E. Charles,[6] C. T. Day,[6] M. S. Gill,[6] A. V. Gritsan,[6] Y. Groysman,[6] R. G. Jacobsen,[6] R. W. Kadel,[6] J. Kadyk,[6] L. T. Kerth,[6] Yu. G. Kolomensky,[6] G. Kukartsev,[6] G. Lynch,[6] L. M. Mir,[6] P. J. Oddone,[6] T. J. Orimoto,[6] M. Pripstein,[6] N. A. Roe,[6] M. T. Ronan,[6] W. A. Wenzel,[6] M. Barrett,[7] K. E. Ford,[7] T. J. Harrison,[7] A. J. Hart,[7] C. M. Hawkes,[7] S. E. Morgan,[7] A. T. Watson,[7] M. Fritsch,[8] K. Goetzen,[8] T. Held,[8] H. Koch,[8] B. Lewandowski,[8] M. Pelizaeus,[8] K. Peters,[8] T. Schroeder,[8] M. Steinke,[8] J. T. Boyd,[9] J. P. Burke,[9] N. Chevalier,[9] W. N. Cottingham,[9] T. Cuhadar-Donszelmann,[10] B. G. Fulsom,[10] C. Hearty,[10] N. S. Knecht,[10] T. S. Mattison,[10] J. A. McKenna,[10] A. Khan,[11] P. Kyberd,[11] M. Saleem,[11] L. Teodorescu,[11] A. E. Blinov,[12] V. E. Blinov,[12] A. D. Bukin,[12] V. P. Druzhinin,[12] V. B. Golubev,[12] E. A. Kravchenko,[12] A. P. Onuchin,[12] S. I. Serednyakov,[12] Yu. I. Skovpen,[12] E. P. Solodov,[12] A. N. Yushkov,[12] D. Best,[13] M. Bondioli,[13] M. Bruinsma,[13] M. Chao,[13] S. Curry,[13] I. Eschrich,[13] D. Kirkby,[13] A. J. Lankford,[13] P. Lund,[13] M. Mandelkern,[13] R. K. Mommsen,[13] W. Roethel,[13] D. P. Stoker,[13] C. Buchanan,[14] B. L. Hartfiel,[14] A. J. R. Weinstein,[14] S. D. Foulkes,[15] J. W. Gary,[15] O. Long,[15] B. C. Shen,[15] K. Wang,[15] L. Zhang,[15] D. del Re,[16] H. K. Hadavand,[16] E. J. Hill,[16] D. B. MacFarlane,[16] H. P. Paar,[16] S. Rahatlou,[16] V. Sharma,[16] J. W. Berryhill,[17] C. Campagnari,[17] A. Cunha,[17] B. Dahmes,[17] T. M. Hong,[17] M. A. Mazur,[17] J. D. Richman,[17] W. Verkerke,[17] T. W. Beck,[18] A. M. Eisner,[18] C. J. Flacco,[18] C. A. Heusch,[18] J. Kroseberg,[18] W. S. Lockman,[18] G. Nesom,[18] T. Schalk,[18] B. A. Schumm,[18] A. Seiden,[18] P. Spradlin,[18] D. C. Williams,[18] M. G. Wilson,[18] J. Albert,[19] E. Chen,[19] G. P. Dubois-Felsmann,[19] A. Dvoretskii,[19] D. G. Hitlin,[19] I. Narsky,[19] T. Piatenko,[19] F. C. Porter,[19] A. Ryd,[19] A. Samuel,[19] R. Andreassen,[20] S. Jayatilleke,[20] G. Mancinelli,[20] B. T. Meadows,[20] M. D. Sokoloff,[20] F. Blanc,[21] P. Bloom,[21] S. Chen,[21] W. T. Ford,[21] J. F. Hirschauer,[21] A. Kreisel,[21] U. Nauenberg,[21] A. Olivas,[21] P. Rankin,[21] W. O. Ruddick,[21] J. G. Smith,[21] K. A. Ulmer,[21] S. R. Wagner,[21] J. Zhang,[21] A. Chen,[22] E. A. Eckhart,[22] A. Soffer,[22] W. H. Toki,[22] R. J. Wilson,[22] Q. Zeng,[22] D. Altenburg,[23] E. Feltresi,[23] A. Hauke,[23] B. Spaan,[23] T. Brandt,[24] J. Brose,[24] M. Dickopp,[24] V. Klose,[24] H. M. Lacker,[24] R. Nogowski,[24] S. Otto,[24] A. Petzold,[24] G. Schott,[24] J. Schubert,[24] K. R. Schubert,[24] R. Schwierz,[24] J. E. Sundermann,[24] D. Bernard,[25] G. R. Bonneaud,[25] P. Grenier,[25] S. Schrenk,[25] Ch. Thiebaux,[25] G. Vasileiadis,[25] M. Verderi,[25] D. J. Bard,[26] P. J. Clark,[26] W. Gradl,[26] F. Muheim,[26] S. Playfer,[26] Y. Xie,[26] M. Andreotti,[27] V. Azzolini,[27] D. Bettoni,[27] C. Bozzi,[27] R. Calabrese,[27] G. Cibinetto,[27] E. Luppi,[27] M. Negrini,[27] L. Piemontese,[27] F. Anulli,[28] R. Baldini-Ferroli,[28] A. Calcaterra,[28] R. de Sangro,[28] G. Finocchiaro,[28] P. Patteri,[28] I. M. Peruzzi,[28,*] M. Piccolo,[28] A. Zallo,[28] A. Buzzo,[29] R. Capra,[29] R. Contri,[29] M. Lo Vetere,[29] M. Macri,[29] M. R. Monge,[29] S. Passaggio,[29] C. Patrignani,[29] E. Robutti,[29] A. Santroni,[29] S. Tosi,[29] G. Brandenburg,[30] K. S. Chaisanguanthum,[30] M. Morii,[30] E. Won,[30] J. Wu,[30] R. S. Dubitzky,[31] U. Langenegger,[31] J. Marks,[31] S. Schenk,[31] U. Uwer,[31] W. Bhimji,[32] D. A. Bowerman,[32] P. D. Dauncey,[32] U. Egede,[32] R. L. Flack,[32] J. R. Gaillard,[32] G. W. Morton,[32] J. A. Nash,[32] M. B. Nikolich,[32] G. P. Taylor,[32] W. P. Vazquez,[32] M. J. Charles,[33] W. F. Mader,[33] U. Mallik,[33] A. K. Mohapatra,[33] J. Cochran,[34] H. B. Crawley,[34] V. Eyges,[34] W. T. Meyer,[34] S. Prell,[34] E. I. Rosenberg,[34] A. E. Rubin,[34] J. Yi,[34] N. Arnaud,[35] M. Davier,[35] X. Giroux,[35] G. Grosdidier,[35] A. Höcker,[35] F. Le Diberder,[35] V. Lepeltier,[35] A. M. Lutz,[35] A. Oyanguren,[35] T. C. Petersen,[35] M. Pierini,[35] S. Plaszczynski,[35] S. Rodier,[35] P. Roudeau,[35] M. H. Schune,[35] A. Stocchi,[35] G. Wormser,[35] C. H. Cheng,[36] D. J. Lange,[36] M. C. Simani,[36] D. M. Wright,[36] A. J. Bevan,[37] C. A. Chavez,[37] I. J. Forster,[37] J. R. Fry,[37] E. Gabathuler,[37] R. Gamet,[37] K. A. George,[37] D. E. Hutchcroft,[37] R. J. Parry,[37] D. J. Payne,[37] K. C. Schofield,[37] C. Touramanis,[37] C. M. Cormack,[38] F. Di Lodovico,[38] W. Menges,[38] R. Sacco,[38] C. L. Brown,[39] G. Cowan,[39] H. U. Flaecher,[39] M. G. Green,[39] D. A. Hopkins,[39] P. S. Jackson,[39] T. R. McMahon,[39] S. Ricciardi,[39] F. Salvatore,[39] D. Brown,[40] C. L. Davis,[40] J. Allison,[41] N. R. Barlow,[41] R. J. Barlow,[41] C. L. Edgar,[41] M. C. Hodgkinson,[41] M. P. Kelly,[41] G. D. Lafferty,[41] M. T. Naisbit,[41] J. C. Williams,[41] C. Chen,[42] W. D. Hulsbergen,[42] A. Jawahery,[42] D. Kovalskyi,[42] C. K. Lae,[42] D. A. Roberts,[42] G. Simi,[42] G. Blaylock,[43] C. Dallapiccola,[43] S. S. Hertzbach,[43] R. Kofler,[43] V. B. Koptchev,[43] X. Li,[43] T. B. Moore,[43] S. Saremi,[43] H. Staengle,[43] S. Willocq,[43] R. Cowan,[44] K. Koeneke,[44] G. Sciolla,[44] S. J. Sekula,[44] M. Spitznagel,[44] F. Taylor,[44] R. K. Yamamoto,[44] H. Kim,[45] P. M. Patel,[45] S. H. Robertson,[45] A. Lazzaro,[46] V. Lombardo,[46] F. Palombo,[46] J. M. Bauer,[47] L. Cremaldi,[47] V. Eschenburg,[47] R. Godang,[47] R. Kroeger,[47] J. Reidy,[47] D. A. Sanders,[47] D. J. Summers,[47] H. W. Zhao,[47] S. Brunet,[48] D. Côté,[48] P. Taras,[48] B. Viaud,[48] H. Nicholson,[49] N. Cavallo,[50,†] G. De Nardo,[50] F. Fabozzi,[50,†] C. Gatto,[50] L. Lista,[50] D. Monorchio,[50] P. Paolucci,[50] D. Piccolo,[50] C. Sciacca,[50] M. Baak,[51] H. Bulten,[51] G. Raven,[51] H. L. Snoek,[51] L. Wilden,[51] C. P. Jessop,[52] J. M. LoSecco,[52]

 

T. Allmendinger,[53] G. Benelli,[53] K. K. Gan,[53] K. Honscheid,[53] D. Hufnagel,[53] P. D. Jackson,[53] H. Kagan,[53] R. Kass,[53] T. Pulliam,[53] A. M. Rahimi,[53] R. Ter-Antonyan,[53] Q. K. Wong,[53] J. Brau,[54] R. Frey,[54] O. Igonkina,[54] M. Lu,[54] C. T. Potter,[54] N. B. Sinev,[54] D. Strom,[54] J. Strube,[54] E. Torrence,[54] F. Galeazzi,[55] M. Margoni,[55] M. Morandin,[55] M. Posocco,[55] M. Rotondo,[55] F. Simonetto,[55] R. Stroili,[55] C. Voci,[55] M. Benayoun,[56] H. Briand,[56] J. Chauveau,[56] P. David,[56] L. Del Buono,[56] Ch. de la Vaissière,[56] O. Hamon,[56] M. J. J. John,[56] Ph. Leruste,[56] J. Malclès,[56] J. Ocariz,[56] L. Roos,[56] G. Therin,[56] P. K. Behera,[57] L. Gladney,[57] Q. H. Guo,[57] J. Panetta,[57] M. Biasini,[58] R. Covarelli,[58] S. Pacetti,[58] M. Pioppi,[58] C. Angelini,[59] G. Batignani,[59] S. Bettarini,[59] F. Bucci,[59] G. Calderini,[59] M. Carpinelli,[59] R. Cenci,[59] F. Forti,[59] M. A. Giorgi,[59] A. Lusiani,[59] G. Marchiori,[59] M. Morganti,[59] N. Neri,[59] E. Paoloni,[59] M. Rama,[59] G. Rizzo,[59] J. Walsh,[59] M. Haire,[60] D. Judd,[60] D. E. Wagoner,[60] J. Biesiada,[61] N. Danielson,[61] P. Elmer,[61] Y. P. Lau,[61] C. Lu,[61] J. Olsen,[61] A. J. S. Smith,[61] A. V. Telnov,[61] F. Bellini,[62] G. Cavoto,[62] A. D'Orazio,[62] E. Di Marco,[62] R. Faccini,[62] F. Ferrarotto,[62] F. Ferroni,[62] M. Gaspero,[62] L. Li Gioi,[62] M. A. Mazzoni,[62] S. Morganti,[62] G. Piredda,[62] F. Polci,[62] F. Safai Tehrani,[62] C. Voena,[62] H. Schröder,[63] G. Wagner,[63] R. Waldi,[63] T. Adye,[64] N. De Groot,[64] B. Franek,[64] G. P. Gopal,[64] E. O. Olaiya,[64] F. F. Wilson,[64] R. Aleksan,[65] S. Emery,[65] A. Gaidot,[65] S. F. Ganzhur,[65] P.-F. Giraud,[65] G. Graziani,[65] G. Hamel de Monchenault,[65] W. Kozanecki,[65] M. Legendre,[65] G. W. London,[65] B. Mayer,[65] G. Vasseur,[65] Ch. Yèche,[65] M. Zito,[65] M. V. Purohit,[66] A. W. Weidemann,[66] J. R. Wilson,[66] F. X. Yumiceva,[66] T. Abe,[67] M. T. Allen,[67] D. Aston,[67] N. van Bakel,[67] R. Bartoldus,[67] N. Berger,[67] A. M. Boyarski,[67] O. L. Buchmueller,[67] R. Claus,[67] J. P. Coleman,[67] M. R. Convery,[67] M. Cristinziani,[67] J. C. Dingfelder,[67] D. Dong,[67] J. Dorfan,[67] D. Dujmic,[67] W. Dunwoodie,[67] S. Fan,[67] R. C. Field,[67] T. Glanzman,[67] S. J. Gowdy,[67] T. Hadig,[67] V. Halyo,[67] C. Hast,[67] T. Hryn'ova,[67] W. R. Innes,[67] M. H. Kelsey,[67] P. Kim,[67] M. L. Kocian,[67] D. W. G. S. Leith,[67] J. Libby,[67] S. Luitz,[67] V. Luth,[67] H. L. Lynch,[67] H. Marsiske,[67] R. Messner,[67] D. R. Muller,[67] C. P. O'Grady,[67] V. E. Ozcan,[67] A. Perazzo,[67] M. Perl,[67] B. N. Ratcliff,[67] A. Roodman,[67] A. A. Salnikov,[67] R. H. Schindler,[67] J. Schwiening,[67] A. Snyder,[67] J. Stelzer,[67] D. Su,[67] M. K. Sullivan,[67] K. Suzuki,[67] S. Swain,[67] J. M. Thompson,[67] J. Va'vra,[67] M. Weaver,[67] W. J. Wisniewski,[67] M. Wittgen,[67] D. H. Wright,[67] A. K. Yarritu,[67] K. Yi,[67] C. C. Young,[67] P. R. Burchat,[68] A. J. Edwards,[68] S. A. Majewski,[68] B. A. Petersen,[68] C. Roat,[68] M. Ahmed,[69] S. Ahmed,[69] M. S. Alam,[69] J. A. Ernst,[69] M. A. Saeed,[69] F. R. Wappler,[69] S. B. Zain,[69] W. Bugg,[70] M. Krishnamurthy,[70] S. M. Spanier,[70] R. Eckmann,[71] J. L. Ritchie,[71] A. Satpathy,[71] R. F. Schwitters,[71] J. M. Izen,[72] I. Kitayama,[72] X. C. Lou,[72] S. Ye,[72] F. Bianchi,[73] M. Bona,[73] F. Gallo,[73] D. Gamba,[73] M. Bomben,[74] L. Bosisio,[74] C. Cartaro,[74] F. Cossutti,[74] G. Della Ricca,[74] S. Dittongo,[74] S. Grancagnolo,[74] L. Lanceri,[74] L. Vitale,[74] F. Martinez-Vidal,[75] R. S. Panvini,[76,‡] Sw. Banerjee,[77] B. Bhuyan,[77] C. M. Brown,[77] D. Fortin,[77] K. Hamano,[77] R. Kowalewski,[77] J. M. Roney,[77] R. J. Sobie,[77] J. J. Back,[78] P. F. Harrison,[78] T. E. Latham,[78] G. B. Mohanty,[78] H. R. Band,[79] X. Chen,[79] B. Cheng,[79] S. Dasu,[79] M. Datta,[79] A. M. Eichenbaum,[79] K. T. Flood,[79] M. Graham,[79] J. J. Hollar,[79] J. R. Johnson,[79] P. E. Kutter,[79] H. Li,[79] R. Liu,[79] B. Mellado,[79] A. Mihalyi,[79] Y. Pan,[79] R. Prepost,[79] P. Tan,[79] J. H. von Wimmersperg-Toeller,[79] S. L. Wu,[79] Z. Yu,[79] and H. Neal[80]

(*BABAR* Collaboration)

[1]*Laboratoire de Physique des Particules, F-74941 Annecy-le-Vieux, France*
[2]*IFAE, Universitat Autonoma de Barcelona, E-08193 Bellaterra, Barcelona, Spain*
[3]*Università di Bari, Dipartimento di Fisica and INFN, I-70126 Bari, Italy*
[4]*Institute of High Energy Physics, Beijing 100039, China*
[5]*University of Bergen, Institute of Physics, N-5007 Bergen, Norway*
[6]*Lawrence Berkeley National Laboratory and University of California, Berkeley, California 94720, USA*
[7]*University of Birmingham, Birmingham, B15 2TT, United Kingdom*
[8]*Ruhr Universität Bochum, Institut für Experimentalphysik 1, D-44780 Bochum, Germany*
[9]*University of Bristol, Bristol BS8 1TL, United Kingdom*
[10]*University of British Columbia, Vancouver, British Columbia, Canada V6T 1Z1*
[11]*Brunel University, Uxbridge, Middlesex UB8 3PH, United Kingdom*
[12]*Budker Institute of Nuclear Physics, Novosibirsk 630090, Russia*
[13]*University of California at Irvine, Irvine, California 92697, USA*
[14]*University of California at Los Angeles, Los Angeles, California 90024, USA*
[15]*University of California at Riverside, Riverside, California 92521, USA*
[16]*University of California at San Diego, La Jolla, California 92093, USA*
[17]*University of California at Santa Barbara, Santa Barbara, California 93106, USA*
[18]*University of California at Santa Cruz, Institute for Particle Physics, Santa Cruz, California 95064, USA*
[19]*California Institute of Technology, Pasadena, California 91125, USA*
[20]*University of Cincinnati, Cincinnati, Ohio 45221, USA*

[21]*University of Colorado, Boulder, Colorado 80309, USA*
[22]*Colorado State University, Fort Collins, Colorado 80523, USA*
[23]*Universität Dortmund, Institut fur Physik, D-44221 Dortmund, Germany*
[24]*Technische Universität Dresden, Institut für Kern- und Teilchenphysik, D-01062 Dresden, Germany*
[25]*Ecole Polytechnique, LLR, F-91128 Palaiseau, France*
[26]*University of Edinburgh, Edinburgh EH9 3JZ, United Kingdom*
[27]*Università di Ferrara, Dipartimento di Fisica and INFN, I-44100 Ferrara, Italy*
[28]*Laboratori Nazionali di Frascati dell'INFN, I-00044 Frascati, Italy*
[29]*Università di Genova, Dipartimento di Fisica and INFN, I-16146 Genova, Italy*
[30]*Harvard University, Cambridge, Massachusetts 02138, USA*
[31]*Universität Heidelberg, Physikalisches Institut, Philosophenweg 12, D-69120 Heidelberg, Germany*
[32]*Imperial College London, London SW7 2AZ, United Kingdom*
[33]*University of Iowa, Iowa City, Iowa 52242, USA*
[34]*Iowa State University, Ames, Iowa 50011-3160, USA*
[35]*Laboratoire de l'Accélérateur Linéaire, F-91898 Orsay, France*
[36]*Lawrence Livermore National Laboratory, Livermore, California 94550, USA*
[37]*University of Liverpool, Liverpool L69 72E, United Kingdom*
[38]*Queen Mary, University of London, London E1 4NS, United Kingdom*
[39]*University of London, Royal Holloway and Bedford New College, Egham, Surrey TW20 0EX, United Kingdom*
[40]*University of Louisville, Louisville, Kentucky 40292, USA*
[41]*University of Manchester, Manchester M13 9PL, United Kingdom*
[42]*University of Maryland, College Park, Maryland 20742, USA*
[43]*University of Massachusetts, Amherst, Massachusetts 01003, USA*
[44]*Massachusetts Institute of Technology, Laboratory for Nuclear Science, Cambridge, Massachusetts 02139, USA*
[45]*McGill University, Montréal, Québec, Canada H3A 2T8*
[46]*Università di Milano, Dipartimento di Fisica and INFN, I-20133 Milano, Italy*
[47]*University of Mississippi, University, Mississippi 38677, USA*
[48]*Université de Montréal, Laboratoire René J. A. Lévesque, Montréal, Québec, Canada H3C 3J7*
[49]*Mount Holyoke College, South Hadley, Massachusetts 01075, USA*
[50]*Università di Napoli Federico II, Dipartimento di Scienze Fisiche and INFN, I-80126, Napoli, Italy*
[51]*NIKHEF, National Institute for Nuclear Physics and High Energy Physics, NL-1009 DB Amsterdam, The Netherlands*
[52]*University of Notre Dame, Notre Dame, Indiana 46556, USA*
[53]*The Ohio State University, Columbus, Ohio 43210, USA*
[54]*University of Oregon, Eugene, Oregon 97403, USA*
[55]*Università di Padova, Dipartimento di Fisica and INFN, I-35131 Padova, Italy*
[56]*Universités Paris VI et VII, Laboratoire de Physique Nucléaire et de Hautes Energies, F-75252 Paris, France*
[57]*University of Pennsylvania, Philadelphia, Pennsylvania 19104, USA*
[58]*Università di Perugia, Dipartimento di Fisica and INFN, I-06100 Perugia, Italy*
[59]*Università di Pisa, Dipartimento di Fisica, Scuola Normale Superiore and INFN, I-56127 Pisa, Italy*
[60]*Prairie View A&M University, Prairie View, Texas 77446, USA*
[61]*Princeton University, Princeton, New Jersey 08544, USA*
[62]*Università di Roma La Sapienza, Dipartimento di Fisica and INFN, I-00185 Roma, Italy*
[63]*Universität Rostock, D-18051 Rostock, Germany*
[64]*Rutherford Appleton Laboratory, Chilton, Didcot, Oxon, OX11 0QX, United Kingdom*
[65]*DSM/Dapnia, CEA/Saclay, F-91191 Gif-sur-Yvette, France*
[66]*University of South Carolina, Columbia, South Carolina 29208, USA*
[67]*Stanford Linear Accelerator Center, Stanford, California 94309, USA*
[68]*Stanford University, Stanford, California 94305-4060, USA*
[69]*State University of New York, Albany, New York 12222, USA*
[70]*University of Tennessee, Knoxville, Tennessee 37996, USA*
[71]*University of Texas at Austin, Austin, Texas 78712, USA*
[72]*University of Texas at Dallas, Richardson, Texas 75083, USA*
[73]*Università di Torino, Dipartimento di Fisica Sperimentale and INFN, I-10125 Torino, Italy*
[74]*Università di Trieste, Dipartimento di Fisica and INFN, I-34127 Trieste, Italy*
[75]*IFIC, Universitat de Valencia-CSIC, E-46071 Valencia, Spain*
[76]*Vanderbilt University, Nashville, Tennessee 37235, USA*

*Also with Università di Perugia, Dipartimento di Fisica, Perugia, Italy.
†Also with Università della Basilicata, Potenza, Italy.
‡Deceased.

[77]*University of Victoria, Victoria, British Columbia, Canada V8W 3P6*
[78]*Department of Physics, University of Warwick, Coventry CV4 7AL, United Kingdom*
[79]*University of Wisconsin, Madison, Wisconsin 53706, USA*
[80]*Yale University, New Haven, Connecticut 06511, USA*
(Received 31 July 2005; published 14 September 2005)

Using 88.9 million $B\overline{B}$ events collected by the *BABAR* detector at the $\Upsilon(4S)$, we measure the branching fraction for the radiative penguin process $B \to X_s\gamma$ from the sum of 38 exclusive final states. The inclusive branching fraction above a minimum photon energy $E_\gamma > 1.9$ GeV is $\mathcal{B}(b \to s\gamma) = (3.27 \pm 0.18(\mathrm{stat})^{+0.55}_{-0.40}(\mathrm{syst})^{+0.04}_{-0.09}(\mathrm{theory})) \times 10^{-4}$. We also measure the isospin asymmetry between $B^- \to X_{s\bar{u}}\gamma$ and $\overline{B}^0 \to X_{s\bar{d}}\gamma$ to be $\Delta_{0-} = -0.006 \pm 0.058(\mathrm{stat}) \pm 0.009(\mathrm{syst}) \pm 0.024(\overline{B}^0/B^-)$. The photon energy spectrum is measured in the $B$ rest frame, from which moments are derived for different values of the minimum photon energy. We present fits to the photon spectrum and moments which give the heavy-quark parameters $m_b$ and $\mu_\pi^2$. The fitted parameters are consistent with those obtained from semileptonic $B \to X_c\ell\nu$ decays, and are useful inputs for the extraction of $|V_{ub}|$ from measurements of semileptonic $B \to X_u\ell\nu$ decays.

DOI: 10.1103/PhysRevD.72.052004 PACS numbers: 13.35.Dx, 11.30.Hv, 14.60.Fg

## I. INTRODUCTION

Radiative decays involving the flavor-changing neutral current transition $b \to s$ are described in the standard model primarily by a one-loop radiative penguin diagram containing a top quark and a $W$ boson. Calculations of this rate in the standard model have now been completed to next-to-leading order (NLO) in $\alpha_s$, with a predicted branching fraction $\mathcal{B}(b \to s\gamma) = (3.57 \pm 0.30) \times 10^{-4}$ for $E_\gamma > 1.6$ GeV [1–3], which is consistent with the current experimental world average $\mathcal{B}(b \to s\gamma) = (3.52^{+0.30}_{-0.28}) \times 10^{-4}$ [4]. Calculations of next-to-next-to-leading order (NNLO) corrections are in progress [5]. Additional contributions to the loop from new physics, e.g. a charged Higgs boson, could change the $b \to s\gamma$ rate [6–10].

The photon energy spectrum in $B \to X_s\gamma$ provides access to the distribution function of the $b$ quark inside the $B$ meson [11]. The knowledge of this shape function is a crucial input in the extraction of $|V_{ub}|$ from inclusive semileptonic $B \to X_u\ell\nu$ measurements [12–17]. We fit the spectrum to two recent predictions, one using a combination of the operator product expansion (OPE) coupled to soft collinear effective theory [3,15–19] in the shape function mass scheme, and the other using a full OPE approach in the kinetic mass scheme [20].

We also present measurements in the $B$ rest frame of the first, second, and third moments of the photon energy spectrum for five different minimum energies, $E_\gamma > 1.90$, 2.00, 2.09, 2.18 and 2.26 GeV. The heavy-quark parameters $m_b$ and $\mu_\pi^2$, which describe the effective $b$ quark mass and kinetic energy inside the $B$ meson, can be determined either from fits to these moments [20], or from the fits to the spectrum. We compare the fitted parameters with those obtained from the lepton energy and hadronic mass moments measured in semileptonic $B \to X_c\ell\nu$ decays [21].

Previous measurements of the inclusive branching fraction have used two different methods. In the fully inclusive method [22–24] the photon energy spectrum is measured without reconstructing the $X_s$ system, and backgrounds are suppressed using information from the rest of the event. When measuring the $E_\gamma$ spectrum inclusively at the $\Upsilon(4S)$ the shape of the spectrum has a large contribution from the 50 MeV calorimeter energy resolution, and from the motion of the $B$ meson in the $\Upsilon(4S)$ rest frame.

The semi-inclusive method [22,25,26] uses a sum of exclusive final states in which possible $X_s$ systems are combined with the photon, and kinematic constraints of $\Upsilon(4S)$ production are used to suppress backgrounds. We have chosen this method and made several improvements over the previous analyses. The number of final states of the $X_s$ system has been increased to 38 by the inclusion of states with two $\pi^0$s, $\eta$ mesons, and three kaons, and the $X_s$ mass range has been increased to 0.6–2.8 GeV. Candidates with correctly reconstructed $X_s$ systems are treated as signal, whereas incorrectly reconstructed systems, referred to as ''cross-feed,'' are treated as background. This method allows us to make a measurement of the branching fraction as a function of the hadronic mass, $M(X_s)$. The $M(X_s)$ spectrum is converted into a high resolution photon energy spectrum using the kinematic relationship for the decay of a $B$ meson of mass $M_B$:

$$E_\gamma = \frac{M_B^2 - M(X_s)^2}{2M_B}, \tag{1}$$

where $E_\gamma$ is the photon energy in the $B$ rest frame which has a resolution of 1–5 MeV.

## II. DETECTOR AND DATA

The results presented in this paper are based on data collected with the *BABAR* detector [27] at the PEP-II asymmetric-energy $e^+e^-$ collider located at the Stanford Linear Accelerator Center. The data sample has an integrated luminosity of 81.9 fb$^{-1}$, corresponding to 88.9 million $B\overline{B}$ pairs recorded at the $\Upsilon(4S)$ resonance (''on-peak,'' center-of-mass energy $\sqrt{s} = 10.58$ GeV). An additional

9.6 fb$^{-1}$ were recorded about 40 MeV below this energy ("off-peak"), for the study of continuum backgrounds in which a light or charm quark pair is produced.

The asymmetric beam configuration in the laboratory frame provides a boost of $\beta\gamma = 0.56$ to the $\Upsilon(4S)$. This results in the high energy photons from $b \to s\gamma$ decays having energies between 1.5 and 4.5 GeV in the laboratory frame. Photons are detected and their energies measured by a CsI(Tl) electromagnetic calorimeter (EMC). The energy scale of the calorimeter crystals is determined by radioactive source and Bhabha scattering calibrations, and the energy leakage of photon showers is corrected using $\pi^0$ decays. The photon energy resolution is measured with symmetric $\pi^0$ and $\eta$ decays to be $\sigma_E/E = \{2.3/E(\mathrm{GeV})^{1/4} \oplus 1.4\}\%$, where the terms are added in quadrature. The measured $\pi^0$ mass resolution is between 6 and 7 MeV for momenta below 1 GeV in the laboratory frame.

Charged particles are detected and their momenta measured by the combination of a silicon vertex tracker, consisting of five layers of double-sided detectors, and a 40-layer central drift chamber, both operating in the 1.5 T magnetic field of a solenoid. The transverse momentum resolution for the tracking system is $\sigma_{p_T}/p_T = 0.0013 p_T \oplus 0.0045$, where $p_T$ is measured in GeV.

Charged particle identification is provided by the average energy loss ($\mathrm{d}E/\mathrm{d}x$) in the tracking devices and by an internally reflecting ring-imaging Cherenkov detector (DIRC). The $\mathrm{d}E/\mathrm{d}x$ resolution from the drift chamber is typically 7.5% for pions. The Cherenkov angle resolution of the DIRC is measured to be 2.4 mrad, which provides more than $3\sigma$ separation between charged kaons and pions up to a momentum of 3 GeV.

## III. $X_S$ SIGNAL MODEL AND BACKGROUNDS

The $B \to X_s\gamma$ signal includes resonant and nonresonant $X_s$ states, but S-wave states are forbidden by angular momentum conservation. It is known experimentally that the mass region $M(X_s) < 1.1$ GeV is dominated by the $K^*(892)$ resonance [28]. In the higher-mass region there is evidence for the $K_1(1270)$ and $K_2^*(1430)$ resonances [29], but these only account for about 16% of the inclusive rate. Theoretical predictions for exclusive decays to higher $K^*$ resonances also account for less than half of the inclusive rate [30].

The sum of many broad resonances can be modeled by an inclusive distribution. In designing our analysis we have used an inclusive calculation from Kagan and Neubert [9]. We follow their prescription and replace the inclusive model in the region $M(X_s) < 1.1$ GeV with an equivalent amount of exclusive $B \to K^*(892)\gamma$. The Kagan and Neubert calculation has two empirical parameters, $m_b$ and $\lambda_1$, which are related to the mean and width of the spectrum (they are similar to the OPE parameters $m_b$ and $-\mu_\pi^2$). The default parameters were originally chosen to be $m_b = 4.65$ GeV and $\lambda_1 = -0.52\mathrm{GeV}^2$, but eventually we fit for these parameters using our measured spectrum. In the inclusive region $M(X_s) = 1.1$–$2.8$ GeV the fragmentation of the $X_s$ system into hadrons is simulated using JETSET [31]. The response of the detector is modeled using GEANT4 [32].

Most of the background in this analysis arises from continuum production of a high energy photon, either by initial state radiation, or from the decays of $\pi^0$ and $\eta$ mesons produced in light-quark jets. We combine event-shape information into a neural network and use the output to remove most of this background. The $\pi^0$ and $\eta$ contributions are further suppressed by vetoes on combinations of the high energy photon with another photon in the event which have a mass consistent with a $\pi^0$ or $\eta$.

Backgrounds from hadronic $b \to c$ decays are important for $M(X_s) > 1.8$ GeV. There are two contributions to this background: combinatorial final states containing particles from both $B$ decays, and incomplete final states where the particles all come from the decay of one $B$, but one or more of the decay products is missing. In the case when only one low energy photon is missing from a $B$ decay to a final state containing a $\pi^0$, e.g. $B \to D^{(*)}\rho^-$, the events tend to peak in the signal region, since only a small amount of energy is missing from the final state. At high hadronic masses this background becomes comparable to the expected signal yield.

Backgrounds from charmless hadronic $B$ decays give a small contribution over the whole $X_s$ mass range, but they include a poorly understood component from $B \to X_s\pi^0$ decays which can peak in the signal region. These backgrounds are modeled as a sum of the measured and yet unmeasured charmless decay modes. There is also a cross-feed background from misreconstructed $B \to X_s\gamma$ decays which is discussed in detail in Sec. V. The requirement of a positively identified kaon removes $B \to X_d\gamma$ decays.

## IV. $B$ MESON RECONSTRUCTION

We reconstruct the $X_s$ states in 38 decay modes and their charge conjugates. This includes 22 final states with a kaon and one to four pions, where at most two of the pions are $\pi^0$s, ten states with a kaon, an $\eta$ and up to two pions, and six states with three kaons plus at most one pion. The kaons can be either $K^-$ or $K_S^0$. A full list of the modes can be found in Table II (below). According to our signal model these modes represent 55% of the total inclusive rate in the region $M(X_s) = 1.1$–$2.8$ GeV. The $X_s$ modes that we do not reconstruct are referred to as "missing fractions."

Neutral kaons are reconstructed as $K_S^0 \to \pi^+\pi^-$ candidates with an invariant mass within 9 MeV of the nominal $K_S^0$ mass [33], and a transverse flight distance greater than 2 mm from the primary event vertex. We do not reconstruct $K_S^0 \to \pi^0\pi^0$ because of its low efficiency, and we do not reconstruct $K_L^0$ because we cannot directly measure its energy. Charged kaons are identified using information from

the DIRC and the tracking devices. The remaining tracks are considered to be from charged pions. Both charged and neutral kaons are required to have momenta $>0.7$ GeV in the laboratory frame. Above this threshold the rate for charged pions to be misidentified as kaons is $<2\%$.

Neutral pions are reconstructed from pairs of photons, each with an energy $>30$ MeV. For $\pi^0$ candidates in the mass interval 117 and 150 MeV, a fit is performed to improve the momentum resolution. To reject combinatorial background, charged and neutral pions are required to have momenta $>0.5$, 0.3, or 0.2 GeV in the laboratory frame for states with 1, 2, or $\geq 3$ pions, respectively.

The $\eta$ mesons are reconstructed from pairs of photons with energies $>50$ MeV. For $\eta$ candidates in the mass interval 520 and 580 MeV, a fit is performed to improve the momentum resolution. The $\eta$ mesons are required to have momenta $>0.7$ GeV in the laboratory frame. We do not explicitly reconstruct the modes $\eta \rightarrow \pi^+\pi^-\pi^0$ and $\eta \rightarrow \pi^0\pi^0\pi^0$, but the former decays are included in the final states with a kaon and $\geq 3$ pions.

The reconstructed $X_s$ system is combined with a high-energy photon to form a $B$ meson. The photon is detected as an isolated energy cluster in the calorimeter, with shape consistent with a single photon, and energy $E^*_\gamma > 1.8$ GeV in the $e^+e^-$ center-of-mass (CM) frame. A veto is applied to high energy photons that, combined with another photon, form either a $\pi^0$ within the mass range 117–150 MeV or an $\eta$ within the mass range 524–566 MeV. In the higher-mass region $M(X_s) > 2.0$ GeV, we improve the rejection of $B \rightarrow D^{(*)}\rho^-$ background by opening up the $\pi^0$ mass window to 106–162 MeV and applying a veto if the $\pi^0$ forms a $\rho^-$ meson in the mass range 400–1200 MeV when combined with a charged pion.

We remove 85% of the continuum background by selections on the angle, $\theta^*_T$, between the thrust axis of the $B$ meson candidate and the thrust axis of all the other particles of the event, requiring $|\cos\theta^*_T| < 0.80$, and the angle, $\theta^*_B$, between the $B$ candidate and the beam axis, requiring $|\cos\theta^*_B| < 0.80$, both defined in the $e^+e^-$ CM system. We then use a neural network to combine information from a set of event-shape variables. The inputs to the neural net include $\theta^*_T$, $\theta^*_B$, $R2$, the ratio of the second to zeroth Fox-Wolfram moments [34], and $R2'$ and $\theta'_T$, which are defined in the primed frame obtained by removing the high energy photon and boosting the rest of the event into its CM frame. These last two variables discriminate against background from initial state radiation. The inputs to the neural net also include a set of 18 energy flow cones each covering an angle of 10° about the reconstructed $B$ direction in the $e^+e^-$ CM system. The neural network selection is tightened above $M(X_s) = 1.1$ GeV, and again above $M(X_s) = 2.0$ GeV and $M(X_s) = 2.4$ GeV, to take account of the increasing background as a function of hadronic mass.

The identification of $B \rightarrow X_s\gamma$ decays makes use of two kinematic variables: the beam-energy substituted mass, $m_{\rm ES} = \sqrt{(\sqrt{s}/2)^2 - p^{*2}_B}$, and the difference between the measured and expected energies of the $B$ candidate, $\Delta E = E^*_B - (\sqrt{s}/2)$, where $E^*_B$ and $p^*_B$ are the energy and momentum of the $B$ candidate in the CM frame, and $\sqrt{s}$ is the total CM energy. When calculating $m_{\rm ES}$, the value of $p^*_B$ is corrected for the tail of the high energy photon response function of the EMC by scaling the measured $E^*_\gamma$ to the value that gives $\Delta E = 0$, the value expected for true signal.

Within an initial selection $m_{\rm ES} > 5.22$ GeV and $|\Delta E| < 0.40$ GeV, we reconstruct two candidates per event on average. In events where more than one $B$ candidate is reconstructed we select the best candidate using the smallest value of $|\Delta E|$. This technique is $>90\%$ efficient when the true $B \rightarrow X_s\gamma$ decay is among the reconstructed candidates. The $|\Delta E|$ distribution has a resolution of about 0.05 GeV with a radiative tail on the low side. For the best candidate we require $|\Delta E| < 0.10$ GeV for $M(X_s) < 2.0$ GeV, and tighten this to $|\Delta E| < 0.08$ GeV for $M(X_s) = 2.0$–$2.4$ GeV and $|\Delta E| < 0.07$ GeV for $M(X_s) = 2.4$–$2.8$ GeV. These selections are optimized to give the best statistical significance for the signal in each $X_s$ region. We then fit the $m_{\rm ES}$ distribution between 5.22 and 5.29 GeV to extract the signal yield.

## V. SIGNAL EFFICIENCY AND CROSS-FEED

The signal efficiency is determined from generated Monte Carlo events which are produced and correctly reconstructed in one of the 38 final states. It does not include the missing $B \rightarrow X_s\gamma$ final states which are discussed in Sec. VII. We generate equal numbers of $B^-$ and $\overline{B}^0$ decays and assume isospin symmetry. The production of $K^-$ and $K^0$ is equal, and the branching fraction for the $K^0_S \rightarrow \pi^+\pi^-$ decay is included in the Monte Carlo generator. For the isospin asymmetry measurement, we note that the efficiency for reconstructing $B^-$ decays is lower than for $\overline{B}^0$ decays by almost a factor of 2. This difference results from a combination of the different distributions of $X_s$ final states and the different efficiencies for $K^0_S$ and $K^-$, $\pi^-$ and $\pi^0$.

The efficiency is a rapidly varying function of hadronic mass. In the $K^*$ region, $M(X_s) < 1.1$ GeV, the efficiency is about 15%, dominated by the high efficiency for reconstructing the $\overline{K}^{*0} \rightarrow K^-\pi^+$ mode. For $M(X_s) > 1.1$ GeV the efficiency decreases from 5% to 1.5% as the hadronic mass increases, as shown in Fig. 1. There are two main reasons for the mass dependence: the multiplicity of the final state particles increases with mass, and the angular correlation between them decreases. In addition, there are steps in efficiency at $M(X_s) = 1.1$, 2.0, and 2.4 GeV because the selection criteria are tightened as the levels of background increase with mass.

The efficiencies that we obtain from the signal samples are corrected for small differences in detection efficiencies between data and Monte Carlo events which are deter-

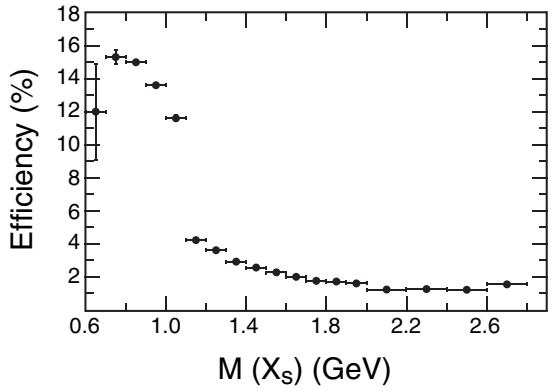


FIG. 1. Efficiency for correctly reconstructing a signal event in one of the 38 final states as a function of hadronic mass. Note that this efficiency does not include the missing fractions of $B \to X_s\gamma$ final states.

mined using control samples. The tracking efficiency is reduced by $(0.8 \pm 2.0)\%$ per track, and the $K_S^0$ efficiency by $(2 \pm 3)\%$. The photon efficiency is not adjusted, but is assigned a 2.5% error per photon. The effect of these adjustments is to reduce the overall signal efficiency by $(1.9 \pm 6.0)\%$. The final state distributions are also adjusted by reweighting the signal Monte Carlo events to match the distributions in data (see Sec. VII).

Monte Carlo events that are reconstructed in a different final state, or with the wrong hadronic mass, are treated as a cross-feed background. The main sources of cross-feed are events from missing final states which are reconstructed in one of the 38 final states, and events from the 38 final states in which one of the final state particles from the $X_s$ is undetected and replaced by a low momentum particle from the other $B$. There is a small contribution from events with multiple candidates in which the true candidate is rejected in favor of another candidate with a smaller value of $|\Delta E|$.

The cross-feed background is fitted together with the hadronic $B$ decay backgrounds, and allowed to have a component that peaks in the signal region. The amount of cross-feed increases as a function of hadronic mass, and is largest for the high multiplicity final states. As part of our systematic studies, we vary the definition of cross-feed, transferring events between the signal and cross-feed samples. This gives changes in background and signal efficiencies which compensate each other within 1%.

## VI. FITTING

To extract the signal yield, we fit the $m_{\rm ES}$ distribution of the data with a combination of a Crystal Ball function [35] for signal, a Novosibirsk function [36] for the peaking backgrounds, and ARGUS functions [37] for the combinatorial backgrounds. The final data fits use $m_{\rm ES}$ shapes derived from fits to three sets of Monte Carlo samples: signal, continuum background, and $B\overline{B}$ background which includes cross-feed. In all cases we use an unbinned maximum likelihood fit.

Figure 2(a) shows the fit to the $m_{\rm ES}$ distribution of correctly reconstructed signal Monte Carlo events with $M(X_s) = 1.4$–$1.5$ GeV. We find no significant variations in the parameters of the Crystal Ball shape over the $M(X_s)$ range, so the values used in the fits to the data are fixed to the weighted average of the results over the full $M(X_s)$ range: a width $\sigma = (2.81 \pm 0.05)$ MeV, a tail parameter $\alpha = 2.17 \pm 0.12$, and a slope $n = 0.99 \pm 0.19$.

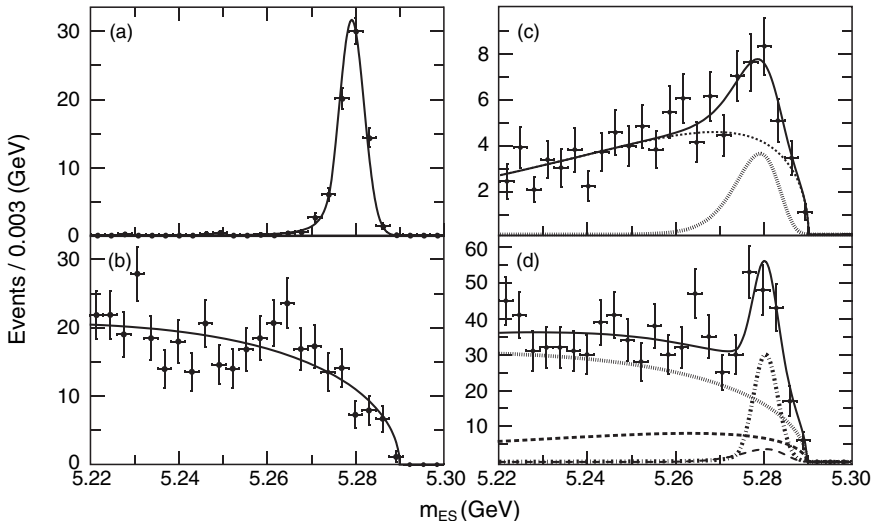


FIG. 2. Fits to the $M(X_s) = 1.4$–$1.5$ GeV bin for (a) correctly reconstructed signal Monte Carlo events; (b) simulated continuum background; (c) simulated cross-feed and hadronic $B$ decay backgrounds, where the contributions from the peaking (dotted) and combinatorial (dashed) backgrounds are shown separately; (d) on-peak data, where the contributions from the signal (dotted-dashed), continuum background (dotted), peaking $B$ background (long-dashed), and combinatorial $B$ background (dashed) are shown separately.

Figure 2(b) shows a fit of an ARGUS function to continuum Monte Carlo events in the same bin in $M(X_s)$. The amount of continuum background increases with $M(X_s)$, and the shape parameter of the ARGUS function is a rapidly varying function of $M(X_s)$. To cross-check our understanding of the continuum background we also fit the off-peak data sample. While the overall variations are well reproduced, we find small systematic differences in both the shape parameter and the normalization which can only be partially accounted for by the difference between the on- and off-peak center-of-mass energies. We fix the continuum ARGUS shapes and normalizations in the fit to the data to the values from the continuum Monte Carlo, which vary from bin to bin, and are adjusted for small offsets observed in comparison to off-peak data. The difference in the normalization between off-peak data and continuum Monte Carlo is 2.8%. These offsets are considered to be part of the systematic errors.

Figure 2(c) shows a fit to the sum of the Monte Carlo predictions for the cross-feed and the hadronic $B$ decay backgrounds using an ARGUS function plus a peaking Novosibirsk function. In the region $M(X_s) < 1.8$ GeV the largest contribution comes from the cross-feed, with only a small contribution from charmless hadronic $B$ decays. In the region $M(X_s) > 1.8$ GeV the hadronic $b \to c$ background increases rapidly. The peaking background shape is broader than the signal shape, reflecting the less-peaked behavior of the backgrounds. The shape of the Novosibirsk function is determined to have $\sigma = 5.0$ MeV and $\tau = -0.295$, from a fit to the simulated $B\overline{B}$ backgrounds over the full $M(X_s)$ range.

TABLE I. Signal yields from the fits to the on-peak data and the $\chi^2$/dof from the fits. Also given are the peaking background yields from fits to cross-feed and $B\bar{B}$ Monte Carlo.

| $M(X_s)$ (GeV) | Data signal yield (events) | Data fit $\chi^2$/dof | Peaking background yield (events) |
|---|---|---|---|
| 0.6–0.7 | 6.5 ± 7.7 | 2.2 | 0.9 ± 3.3 |
| 0.7–0.8 | 5.6 ± 14.1 | 0.8 | 2.7 ± 6.4 |
| 0.8–0.9 | 416.2 ± 23.2 | 1.5 | 24.2 ± 8.5 |
| 0.9–1.0 | 355.6 ± 24.9 | 0.9 | 22.7 ± 10.8 |
| 1.0–1.1 | 51.3 ± 19.0 | 1.0 | 14.4 ± 13.7 |
| 1.1–1.2 | 33.2 ± 12.9 | 1.2 | 7.4 ± 6.0 |
| 1.2–1.3 | 83.2 ± 15.7 | 1.1 | 9.4 ± 7.5 |
| 1.3–1.4 | 101.5 ± 16.8 | 0.8 | 0.8 ± 8.6 |
| 1.4–1.5 | 72.0 ± 15.8 | 0.8 | 15.3 ± 9.1 |
| 1.5–1.6 | 82.4 ± 16.5 | 1.1 | 16.1 ± 11.3 |
| 1.6–1.7 | 66.1 ± 16.9 | 1.0 | 5.3 ± 11.7 |
| 1.7–1.8 | 54.6 ± 16.5 | 1.3 | 5.6 ± 13.1 |
| 1.8–1.9 | 76.6 ± 18.2 | 1.1 | 19.1 ± 13.7 |
| 1.9–2.0 | 13.5 ± 19.5 | 1.1 | 21.3 ± 14.1 |
| 2.0–2.2 | 47.5 ± 21.8 | 0.7 | 19.4 ± 16.8 |
| 2.2–2.4 | 52.1 ± 24.0 | 0.7 | 39.5 ± 21.0 |
| 2.4–2.6 | 44.7 ± 25.6 | 0.8 | 46.8 ± 20.8 |
| 2.6–2.8 | −6.2 ± 31.9 | 1.0 | 81.0 ± 26.1 |
| 0.6–2.8 | 1513.0 ± 85.1 | 1.2 | 464.2 ± 68.3 |

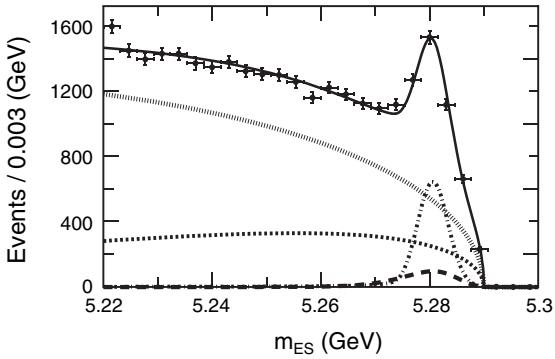


FIG. 3. On-peak data fit to the full $M(X_s)$ range, $M(X_s) =$ 0.6–2.8 GeV bin, where the contributions from the signal shape (dotted-dashed), fixed continuum ARGUS shape (dotted), peaking background shape (long-dashed), and combinatorial $B\overline{B}$ background shape (dashed) are shown separately.

Figure 2(d) shows the fit to the on-peak data in the same mass bin. In this fit the signal yield and the shape and normalization of the combinatorial $B\overline{B}$ background function are allowed to vary. The signal shape is fixed, and the continuum ARGUS function and peaking $B\overline{B}$ background shapes are fixed. The peaking background yield is obtained from the fit shown in Fig. 2(c). Table I gives the fitted signal yields, the peaking $B\overline{B}$ background yields, and, as a measure of the goodness of the maximum likelihood fit, the $\chi^2$ per degree of freedom.

Figure 3 shows the on-peak data fit to the full $M(X_s)$ range, which gives the yield in the last row of Table I. In this fit the continuum ARGUS shape and the peaking $B\overline{B}$ background are taken from fits to the full $M(X_s)$ range of the simulated continuum and $B\overline{B}$ samples.

The fit procedure has been validated with Monte Carlo studies to check for biases in the fitting method. Systematic errors from the fitting method, including variations in the fixed parameters in the fits, are discussed in Sec. VIII.

## VII. $X_s$ FRAGMENTATION AND MISSING FRACTIONS

The fragmentation of the $X_s$ system into hadronic final states has been modeled using JETSET [31]. We check this fragmentation by comparing the observed data yields in the range $M(X_s) = 1.1$–2.8 GeV with the yields expected from the signal Monte Carlo. We do a detailed study by splitting the data and Monte Carlo samples into ten different categories, each containing two to ten of our selected final states. The measured ratios of fitted data signal events to reconstructed Monte Carlo signal events in each category are given in Table II with their statistical errors.

We note that the rates for the $K\pi$ modes are smaller than the JETSET prediction. Also interesting is the low ratio for the final states with three kaons, where we do not observe a

TABLE II. Ratios of data to Monte Carlo yields for various categories of final states. These are used to adjust the fragmentation in the signal Monte Carlo.

| Final states | Data/Monte Carlo |
|---|---|
| $K^-\pi^+$, $K^0_S\pi^-$ | $0.50 \pm 0.07$ |
| $K^-\pi^0$, $K^0_S\pi^0$ | $0.19 \pm 0.12$ |
| $K^-\pi^+\pi^-$, $K^0_S\pi^+\pi^-$ | $1.02 \pm 0.14$ |
| $K^-\pi^+\pi^0$, $K^0_S\pi^-\pi^0$ | $1.34 \pm 0.24$ |
| $K^-\pi^+\pi^-\pi^+$, $K^0_S\pi^+\pi^-\pi^-$ | $2.67 \pm 0.96$ |
| $K^-\pi^+\pi^-\pi^0$, $K^0_S\pi^+\pi^-\pi^0$ | $1.29 \pm 0.61$ |
| $K^-\pi^0\pi^0$, $K^0_S\pi^0\pi^0$<br>$K^-\pi^+\pi^0\pi^0$, $K^0_S\pi^-\pi^0\pi^0$ | $1.89 \pm 1.33$ |
| $K^-\pi^+\pi^-\pi^+\pi^-$, $K^0_S\pi^+\pi^-\pi^+\pi^-$<br>$K^-\pi^+\pi^-\pi^+\pi^0$, $K^0_S\pi^+\pi^-\pi^-\pi^0$<br>$K^-\pi^+\pi^-\pi^0\pi^0$, $K^0_S\pi^+\pi^-\pi^0\pi^0$ | $1.32^{+1.55}_{-1.32}$ |
| $K^-\eta$, $K^0_S\eta$, $K^-\eta\pi^+$<br>$K^0_S\eta\pi^-$, $K^-\eta\pi^0$, $K^0_S\eta\pi^0$<br>$K^-\eta\pi^+\pi^-$, $K^0_S\eta\pi^+\pi^-$<br>$K^-\eta\pi^+\pi^0$, $K^0_S\eta\pi^-\pi^0$ | $0.83^{+1.00}_{-0.83}$ |
| $K^-K^+K^-$, $K^-K^+K^0_S$<br>$K^-K^+K^-\pi^+$, $K^-K^+K^0_S\pi^-$<br>$K^-K^+K^-\pi^0$, $K^-K^+K^0_S\pi^0$ | $0.27^{+0.54}_{-0.27}$ |

significant signal. These differences in fragmentation could be accounted for by changes in the parameters within JETSET, and by the addition of resonant contributions, but a detailed study of this requires a larger data sample.

We also make a comparison of the ratio of $K^0_S$ to $K^-$ final states in data with the same ratio in Monte Carlo. In the range $M(X_s) = 1.1$–$2.8$ GeV this gives a double ratio of $1.00 \pm 0.21$, which is consistent with the assumption of isospin symmetry.

The ratios in Table II are applied as weights to the generated and reconstructed signal Monte Carlo events to correct for the observed fragmentation. The reduction in the $K\pi$ final states and the increase in the high multiplicity final states reduces the signal efficiencies by 10% to 25%, depending on the $M(X_s)$ bin. The weights also lead to an increase in the cross-feed background.

The selected 38 $X_s$ final states do not account for all the states produced in $B \to X_s\gamma$. To obtain the total $B \to X_s\gamma$ branching fraction in each $M(X_s)$ bin, we need to correct for the fraction of missing final states, which increases from 25% to 70% for $M(X_s) = 0.6$ to 2.8 GeV (see Fig. 4). The 25% fraction missing at all hadronic masses comes from $K^0_L$. This fraction is equal to the $K^0_S$ sample, with an uncertainty determined by our isospin asymmetry measurement (see Sec. X).

An analysis of the final states generated in the signal Monte Carlo sample shows that the largest missing contribution comes from high multiplicity final states with a kaon and $\geq 5\pi$. There are also missing contributions of a few percent in the highest mass bins from higher multiplicity final states with $\eta$ mesons, three kaons and baryons. Smaller contributions come from rare radiative meson decays and final state radiation.

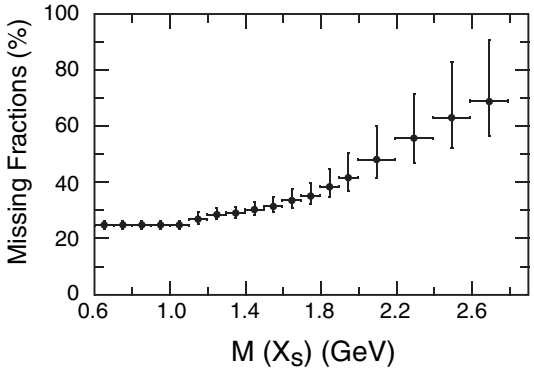


FIG. 4. Missing fractions with systematic errors as a function of the hadronic mass.

We use the results of the fragmentation study to correct for the missing high multiplicity states with $\eta$ and three kaons with the weights found for the observed final states. Since the kaon and $4\pi$ modes are consistent with the Monte Carlo expectation within a large statistical error, we do not adjust the fractions of kaon and $\geq 5\pi$ modes. For these final states, and for missing fractions where there is no information from the reconstructed final states, we assign systematic errors which allow the missing fraction to vary by a factor two relative to the predicted value. The uncertainty in the missing fractions is the dominant systematic error in the high mass bins.

## VIII. SYSTEMATICS

The following systematic errors are independent of $M(X_s)$. There is a 1.1% uncertainty in our knowledge of the number of $B$ mesons in our data sample. There is a 2.5% uncertainty in the efficiency of the initial selection of the high energy photon, but we apply additional criteria to isolate the high energy photon, as well as vetoes if it forms a $\pi^0$ or $\eta$ meson. The efficiency of these additional selections is checked using the $K^*\gamma$ region as a control sample, and we assign an additional uncertainty of 1.5%. The total systematic error independent of $M(X_s)$ is 3.1%.

The systematic errors that depend on $M(X_s)$ are summarized in Table III. There are several different categories of systematic errors associated with detection efficiencies, fitting, the modeling of peaking backgrounds, fragmentation corrections, and the estimation of the missing fractions.

The detection efficiency errors come from our knowledge of the differences between Monte Carlo and data obtained from control samples. They reflect the accuracy of our modeling of the detector response, and include tracking efficiency (2%), particle identification for charged

TABLE III. Contributions to the $M(X_s)$-dependent systematic error on the branching fraction from detection efficiency, fitting, peaking background, fragmentation and missing fractions are shown in % as a function of hadronic mass. The total systematic errors also include a 3.1% systematic error that is independent of $M(X_s)$ and not listed in the table.

| $M(X_s)$ (GeV) | Detector efficiency | Fitting | Peaking background | Fragmentation | Missing fraction | Total |
|---|---|---|---|---|---|---|
| 0.6–0.7 | 5.2 | $^{+20.8}_{-21.4}$ | 8.1 | | $^{+1.8}_{-2.0}$ | $^{+23.1}_{-23.6}$ |
| 0.7–0.8 | 5.3 | $^{+33.1}_{-41.0}$ | 2.5 | | $^{+1.8}_{-2.0}$ | $^{+33.7}_{-41.4}$ |
| 0.8–0.9 | 5.4 | $^{+2.3}_{-2.3}$ | 1.1 | | $^{+1.8}_{-2.0}$ | $^{+6.6}_{-6.6}$ |
| 0.9–1.0 | 5.3 | $^{+2.2}_{-2.2}$ | 0.8 | | $^{+1.8}_{-2.0}$ | $^{+6.4}_{-6.4}$ |
| 1.0–1.1 | 5.3 | $^{+10.2}_{-10.4}$ | 3.2 | 13.7 | $^{+2.6}_{-2.2}$ | $^{+18.5}_{-18.5}$ |
| 1.1–1.2 | 6.2 | $^{+11.1}_{-11.2}$ | 1.7 | 5.4 | $^{+3.4}_{-2.5}$ | $^{+14.5}_{-14.4}$ |
| 1.2–1.3 | 6.4 | $^{+5.5}_{-5.6}$ | 1.8 | 4.5 | $^{+3.4}_{-2.4}$ | $^{+10.5}_{-10.3}$ |
| 1.3–1.4 | 6.6 | $^{+4.3}_{-4.5}$ | 1.8 | 4.5 | $^{+3.3}_{-2.4}$ | $^{+10.0}_{-9.8}$ |
| 1.4–1.5 | 6.7 | $^{+4.6}_{-4.7}$ | 2.1 | 5.8 | $^{+3.9}_{-2.8}$ | $^{+11.1}_{-10.8}$ |
| 1.5–1.6 | 6.9 | $^{+2.1}_{-2.4}$ | 2.9 | 4.9 | $^{+4.7}_{-3.0}$ | $^{+10.5}_{-9.9}$ |
| 1.6–1.7 | 7.0 | $^{+3.1}_{-3.5}$ | 4.0 | 5.3 | $^{+6.1}_{-3.9}$ | $^{+12.0}_{-11.1}$ |
| 1.7–1.8 | 7.1 | $^{+4.1}_{-4.2}$ | 2.0 | 5.5 | $^{+7.5}_{-4.5}$ | $^{+12.7}_{-11.2}$ |
| 1.8–1.9 | 7.2 | $^{+3.2}_{-3.4}$ | 2.2 | 6.5 | $^{+10.6}_{-5.9}$ | $^{+15.0}_{-12.2}$ |
| 1.9–2.0 | 7.1 | $^{+32.6}_{-32.4}$ | 9.3 | 5.4 | $^{+15.0}_{-8.0}$ | $^{+38.2}_{-35.8}$ |
| 2.0–2.2 | 7.2 | $^{+11.6}_{-9.4}$ | 5.1 | 6.2 | $^{+23.4}_{-12.7}$ | $^{+28.3}_{-19.2}$ |
| 2.2–2.4 | 7.5 | $^{+10.8}_{-9.1}$ | 8.9 | 7.1 | $^{+36.2}_{-19.8}$ | $^{+40.2}_{-25.8}$ |
| 2.4–2.6 | 7.5 | $^{+7.6}_{-7.6}$ | 11.1 | 9.3 | $^{+55.2}_{-29.7}$ | $^{+58.1}_{-34.8}$ |
| 2.6–2.8 | 7.9 | $^{+68.3}_{-96.1}$ | 65.7 | 11.7 | $^{+71.3}_{-39.9}$ | $^{+119.0}_{-124.0}$ |
| 0.6–2.8 | 6.1 | $^{+3.2}_{-3.7}$ | 1.6 | 5.9 | $^{+13.8}_{-7.6}$ | $^{+16.7}_{-12.2}$ |

kaons (1%), $K^0_S$ reconstruction (3%), and photon detection efficiency (2.5%). These differences give not only systematic errors but also shifts in the signal detection efficiencies, as mentioned in Sec. V. The fitting errors come from varying the fixed parameters in the data fits. The signal peak position in $m_{ES}$ is varied by $\pm 0.4$ MeV, and the width by $\pm 0.1$ MeV to allow for a possible variation as a function of $M(X_s)$. The width is varied in a correlated fashion with the $\alpha$ and tail parameters of the Crystal Ball function. These changes in the signal shape alter the signal yields by between 0 and 5 events in each $M(X_s)$ bin. The peaking background shape is varied within a range allowed by the cross-feed and $B\overline{B}$ Monte Carlo samples. This gives smaller changes in the signal yield of about one event in each bin. The continuum shape and normalization are varied by the difference between the continuum Monte Carlo and the off-peak data, but this gives very small changes in the signal yields.

The peaking background normalization error is treated separately. In the region $M(X_s) < 1.8$ GeV the main uncertainty comes from the charmless hadronic decays $B \to X_s \pi^0$. While some of these have been measured, others are yet to be observed. Combining the effects of the measured and the unmeasured modes we assign an uncertainty of 50% to the normalization of this contribution in the low $M(X_s)$ region. In the region $M(X_s) > 1.8$ GeV the background is primarily from hadronic $b \to c$ decays, such as $B \to D^* \rho^-$. By taking the weighted average of the uncertainties on the branching fractions of the components of this background, we assign an uncertainty of 15% to the normalization of this contribution in the high $M(X_s)$ region. The cross-feed background depends on the modeling of the $B \to X_s \gamma$ process. We use the fragmentation weights and the measured spectral shape to adjust the signal Monte Carlo to match the data, correct our prediction for the peaking cross-feed background, and assign an uncertainty to this correction.

As discussed in Sec. VII, we have studied the differences in fragmentation between data and signal Monte Carlo, and reweighted the signal Monte Carlo to correct for the differences found. The weighting factors are listed by category in Table II. We vary the weights by their statistical errors to evaluate the fragmentation systematics. For the $\eta$ and $K + 4\pi$ categories, the weights are consistent with one (with larger errors), and we restrict the range to be between 0.5 and 2.0. Each weight is varied separately, and assumed to be uncorrelated with the other weights. The fragmentation errors are limited by the statistics of the data sample. In the bin $M(X_s) = 1.0$–$1.1$ GeV the efficiency is computed from the average of the resonant and nonresonant

model efficiencies, and we take the difference between them as an additional fragmentation systematic of 12.8% in this bin.

The estimation of the missing fractions is the largest systematic error. It is determined by varying the missing fractions within the ranges shown in Fig. 4. We vary all the uncertainties in the missing fractions together, either increasing them all or decreasing them all. When we do this we adjust the sum of the reconstructed final states so that the total $B \to X_s\gamma$ rate is unchanged, i.e. we actually adjust the relative proportions of reconstructed and missing final states.

## IX. BRANCHING FRACTION RESULTS

The branching fractions in each hadronic mass bin are obtained using the signal efficiencies shown in Fig. 1, the signal yields given in Table I, the fraction of reconstructed final states (which is 1 minus the fraction of missing final states shown in Fig. 4), and the total number of $B\overline{B}$ pairs in the sample. The systematic studies which affect each of these quantities were discussed in Sec. VIII.

Table IV shows the results for the branching fraction in each hadronic mass bin, as well as the result for the whole mass range. Table V shows the corresponding branching fractions in bins of the photon energy using Eq. (1) to translate between hadronic mass and photon energy. We have taken into account the different bin sizes in transforming between $\mathcal{B}(M(X_s))$ and $\mathcal{B}(E_\gamma)$. The corresponding hadronic mass and photon energy spectra are shown in Fig. 5, where theoretical predictions are shown which will be discussed in Sec. XI. The hadronic mass resolution

TABLE IV. Branching fractions in bins of hadronic mass with statistical and systematic errors. The bottom line shows the total branching fraction obtained from the separate fit to the data over the full $M(X_s)$ range, and not from the sum of the individual bins.

| $M(X_s)$ (GeV) | $\mathcal{B}(M(X_s))/100$ MeV $(10^{-6})$ |
|---|---|
| 0.6–0.7 | $0.4 \pm 0.5^{+0.1}_{-0.1}$ |
| 0.7–0.8 | $0.3 \pm 0.7^{+0.1}_{-0.1}$ |
| 0.8–0.9 | $20.8 \pm 1.2^{+1.3}_{-1.3}$ |
| 0.9–1.0 | $19.6 \pm 1.4^{+1.2}_{-1.2}$ |
| 1.0–1.1 | $3.3 \pm 1.2^{+0.6}_{-0.6}$ |
| 1.1–1.2 | $6.2 \pm 2.4^{+0.9}_{-0.9}$ |
| 1.2–1.3 | $18.1 \pm 3.4^{+1.9}_{-1.9}$ |
| 1.3–1.4 | $27.6 \pm 4.6^{+2.8}_{-2.7}$ |
| 1.4–1.5 | $22.6 \pm 5.0^{+2.5}_{-2.5}$ |
| 1.5–1.6 | $29.8 \pm 6.0^{+3.1}_{-3.0}$ |
| 1.6–1.7 | $28.0 \pm 7.2^{+3.3}_{-3.1}$ |
| 1.7–1.8 | $26.9 \pm 8.1^{+3.4}_{-3.0}$ |
| 1.8–1.9 | $40.6 \pm 9.7^{+6.1}_{-5.0}$ |
| 1.9–2.0 | $8.0 \pm 11.7^{+3.1}_{-2.9}$ |
| 2.0–2.2 | $21.0 \pm 9.6^{+5.9}_{-4.0}$ |
| 2.2–2.4 | $26.1 \pm 12.0^{+10.5}_{-6.7}$ |
| 2.4–2.6 | $28.0 \pm 16.0^{+16.2}_{-9.7}$ |
| 2.6–2.8 | $-3.7 \pm 18.8^{+4.4}_{-4.5}$ |
| | $\mathcal{B}(10^{-6})$ |
| 0.6–2.8 | $327.0 \pm 18.0^{+55.0}_{-40.0}$ |

TABLE V. Branching fractions in bins of photon energy with statistical and systematic errors.

| $E_\gamma$ (GeV) | $\mathcal{B}(E_\gamma)/100$ MeV $(10^{-6})$ |
|---|---|
| 2.593–2.606 | $3.3 \pm 4.0^{+0.8}_{-0.8}$ |
| 2.579–2.593 | $1.9 \pm 4.9^{+0.6}_{-0.8}$ |
| 2.563–2.579 | $129.2 \pm 7.2^{+8.1}_{-8.1}$ |
| 2.545–2.563 | $108.9 \pm 7.6^{+6.6}_{-6.6}$ |
| 2.525–2.545 | $16.7 \pm 6.2^{+3.2}_{-3.2}$ |
| 2.503–2.525 | $28.6 \pm 11.1^{+4.1}_{-4.1}$ |
| 2.480–2.503 | $76.3 \pm 14.4^{+8.0}_{-7.8}$ |
| 2.454–2.480 | $107.8 \pm 17.9^{+10.8}_{-10.6}$ |
| 2.427–2.454 | $82.4 \pm 18.1^{+9.2}_{-8.9}$ |
| 2.397–2.427 | $101.6 \pm 20.3^{+10.6}_{-10.1}$ |
| 2.366–2.397 | $89.5 \pm 22.9^{+10.7}_{-9.9}$ |
| 2.333–2.366 | $81.3 \pm 24.6^{+10.3}_{-9.1}$ |
| 2.298–2.333 | $115.8 \pm 27.6^{+17.4}_{-14.1}$ |
| 2.261–2.298 | $21.8 \pm 31.6^{+8.3}_{-7.8}$ |
| 2.181–2.261 | $52.7 \pm 24.2^{+14.9}_{-10.1}$ |
| 2.094–2.181 | $60.0 \pm 27.6^{+24.1}_{-15.5}$ |
| 1.999–2.094 | $59.0 \pm 33.8^{+34.3}_{-20.5}$ |
| 1.897–1.999 | $-7.1 \pm 36.7^{+8.5}_{-8.8}$ |

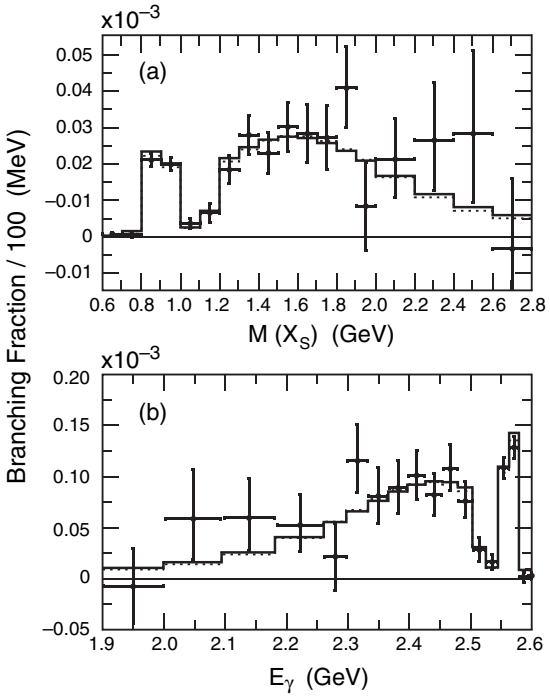


FIG. 5. The hadronic mass spectrum (a), and the photon energy spectrum (b). The data points are compared to theoretical predictions (histograms) obtained using the shape function (solid line) and kinetic (dashed line) schemes.

of 10 MeV converts into an $E_\gamma$ resolution of 1–5 MeV, and the $K^*$ peak can be clearly seen in both the hadronic mass and photon energy spectra.

## X. ISOSPIN ASYMMETRY

We define the isospin asymmetry as the ratio:

$$\Delta_{0-} = \frac{\Gamma(\overline{B}^0 \to X_{s\bar{d}}\gamma) - \Gamma(B^- \to X_{s\bar{u}}\gamma)}{\Gamma(\overline{B}^0 \to X_{s\bar{d}}\gamma) + \Gamma(B^- \to X_{s\bar{u}}\gamma)}. \quad (2)$$

The standard model predicts no isospin symmetry breaking from the dominant penguin diagram for $B \to X_s\gamma$. Isospin symmetry-breaking effects occur at order $\Lambda/m_b$ in the heavy-quark expansion [38], due to annihilation contributions from four-quark operators, the chromomagnetic dipole operator and charm penguins. For the exclusive decays $B \to K^*\gamma$, the standard model predicts a positive value of $\Delta_{0-}$ between 5% and 10% [38], but new physics beyond the standard model could enhance the isospin breaking effects. Measurements of the $B \to K^*\gamma$ isospin asymmetry from *BABAR* and BELLE are consistent with the predictions of the standard model [28].

We split the 38 modes into charged and neutral $B$ decays, refit the data, and calculate the separate efficiencies and total branching fractions. While the signal detection efficiencies are almost a factor of 2 lower for the $B^-$ decays, the backgrounds and missing fractions are symmetric. Comparing the charged and neutral branching fraction measurements, using the lifetime ratio, $\tau(B^-)/\tau(B^0) = 1.086 \pm 0.017$ [33], and our recent measurement of the production ratio of charged and neutral $B$ events at the $\Upsilon(4S)$, $\overline{B}^0/B^- = 1.006 \pm 0.048$ [39], gives the isospin asymmetry over the range $M(X_s) =$ 0.6–2.8 GeV:

$$\Delta_{0-} = -0.006 \pm 0.058 \pm 0.009 \pm 0.024.$$

The errors are statistical, systematic, and due to the production ratio $\overline{B}^0/B^-$, respectively. Most of the systematic errors on the branching fractions cancel in the ratio. The residual systematic errors that are relevant to the isospin asymmetry are $\pm 0.001$ from the detection efficiency corrections, and $+0.004$ from a study of the fragmentation differences between charged and neutral $B$ modes in which we allow for different $B^-$ and $\overline{B}^0$ weights. The largest contribution to our systematic error is $\pm 0.008$ due to the uncertainty in the lifetime ratio.

## XI. FITS TO THE SPECTRUM, EXTRACTION OF $m_b$ AND $\mu_\pi^2$, AND INCLUSIVE BRANCHING FRACTION

In the following section, we evaluate the results in the context of recent QCD calculations in the shape function [3,15–19] and kinetic [20] schemes. From a fit to the spectrum, we evaluate the $b$-quark mass $m_b(\mu)$, and the kinetic-energy parameter $\mu_\pi^2(\mu)$, where the reference scales are taken to be $\mu = 1.5$ GeV in the shape function scheme, and $\mu = 1.0$ GeV in the kinetic scheme. We have set the chromomagnetic operator $\mu_G = 0.35\ \mathrm{GeV}^2$, and the Darwin and spin-orbit operators to $\rho_D = 0.2\ \mathrm{GeV}^3$ and $\rho_{LS} = -0.09\ \mathrm{GeV}^3$ in the kinetic scheme [40]. The photon and hadronic mass spectra are equivalent, so we can fit either one to extract the heavy-quark parameters.

We use a $\chi^2$ method to fit the spectrum and find the best values of the parameters $m_b$ and $\mu_\pi^2$, adding an additional constraint on the normalization of the spectrum from the value of $\mathcal{B}(b \to s\gamma)$ measured over the full range $M(X_s) =$ 0.6–2.8 GeV. The fit method takes into account the asymmetry of the systematic errors and the large bin-to-bin correlations.

The spectrum is fit using the expected spectral shape from the two schemes, except that at low hadronic mass we replace the inclusive theoretical distribution with a Breit-Wigner to represent the $K^*$ resonance. The transition point between the $K^*$ and inclusive distributions is a free parameter of the fit. As a cross-check we have also performed fits to the spectrum where we treat the $K^*$ region $M(X_s) =$ 0.6–1.2 GeV as a single bin. In this case a Breit-Wigner shape and a transition point are unnecessary to describe the data. The results of this cross-check agree with the default fits with the $K^*$ included.

The signal Monte Carlo, which is used to determine the signal efficiencies and the cross-feed background, depends on the mass scheme used and the corresponding heavy-quark parameters. Starting from the initial fits to the measured spectrum, we modify the signal Monte Carlo with the fitted parameters, and revise our estimates of efficiencies and cross-feed. We refit the data, recalculate the branching fractions, and then refit the spectrum. This procedure leads to small changes in the heavy-quark parameters which are well within the errors.

The final results after the refitting are shown in Table VI for $m_b$ and $\mu_\pi^2$. In the shape function scheme, we present results using three different models for the shape function [17]. The exponential and hyperbolic models give very similar results, and the exponential model is taken to be the default in this scheme. Slightly different results are obtained with the Gaussian model. In the kinetic scheme, we use the two functions provided by the authors, and quote the average [40]. We show the fits to the measured hadronic mass and photon energy spectrum in Fig. 5, from which it can be seen that the spectrum is well described and the difference between the two schemes is small. The central values and error ellipses for the shape function scheme of the fitted heavy-quark parameters are shown in Fig. 6 (the points of the exponential model ellipse are given in the appendix). For comparison with previous measurements we have also fitted the spectrum to the older model of Kagan and Neubert [9]. We find $m_b = (4.79^{+0.06}_{-0.10})\ \mathrm{GeV}$ for the $b$ quark mass and $\lambda_1 = (-0.24^{+0.09}_{-0.18})\ \mathrm{GeV}^2$ for the kinetic parameter, with a 94% correlation between them.

TABLE VI. Heavy-quark parameters $m_b$ and $\mu_\pi^2$ from fits to the spectrum using the three different models of the shape function scheme and using the kinetic scheme. For each scheme the first two columns are from a fit with just statistical errors, and the last two columns from a fit with statistical and systematic errors. The correlation coefficients between the two parameters are $-94\%$ and $-92\%$ in the two schemes.

| Theoretical scheme | Statistical errors | | Statistical + Systematic errors | |
|---|---|---|---|---|
| | $m_b$(GeV) | $\mu_\pi^2$(GeV$^2$) | $m_b$(GeV) | $\mu_\pi^2$(GeV$^2$) |
| Shape function | | | | |
| Exponential | $4.65 \pm 0.04$ | $0.19 \pm 0.06$ | $4.67 \pm 0.07$ | $0.16^{+0.10}_{-0.08}$ |
| Hyperbolic | $4.64 \pm 0.04$ | $0.20 \pm 0.06$ | $4.67 \pm 0.07$ | $0.17^{+0.10}_{-0.09}$ |
| Gaussian | $4.68 \pm 0.04$ | $0.12 \pm 0.06$ | $4.73^{+0.06}_{-0.07}$ | $0.07^{+0.09}_{-0.06}$ |
| Kinetic | $4.67 \pm 0.04$ | $0.32^{+0.07}_{-0.04}$ | $4.70^{+0.04}_{-0.08}$ | $0.29^{+0.09}_{-0.04}$ |

The inclusive branching fraction is obtained from a fit to the $m_{\rm ES}$ distribution of data events over the full $M(X_s)$ range, corresponding to $E_\gamma > 1.90$ GeV (Fig. 3). In the shape function scheme we obtain $\mathcal{B}(b \to s\gamma) = (3.27 \pm 0.18^{+0.55+0.04}_{-0.40-0.06}) \times 10^{-4}$ and in the kinetic scheme $\mathcal{B}(b \to s\gamma) = (3.27 \pm 0.18^{+0.55+0.04}_{-0.40-0.12}) \times 10^{-4}$. The errors are, respectively, statistical, systematic, and due to the variation of the shape parameters. We quote the average of the results from the two theoretical schemes:

$$\mathcal{B}(b \to s\gamma) = (3.27 \pm 0.18^{+0.55+0.04}_{-0.40-0.09}) \times 10^{-4},$$
$$E_\gamma > 1.9 \text{ GeV}.$$

The branching fraction can be extrapolated to a lower photon energy using the fits to the spectrum. Again we quote the average of the two schemes:

$$\mathcal{B}(b \to s\gamma) = (3.35 \pm 0.19^{+0.56+0.04}_{-0.41-0.09}) \times 10^{-4},$$
$$E_\gamma > 1.6 \text{ GeV},$$

where the small uncertainties from the extrapolations in the two schemes enter into the model error through the variation of the fitted parameters.

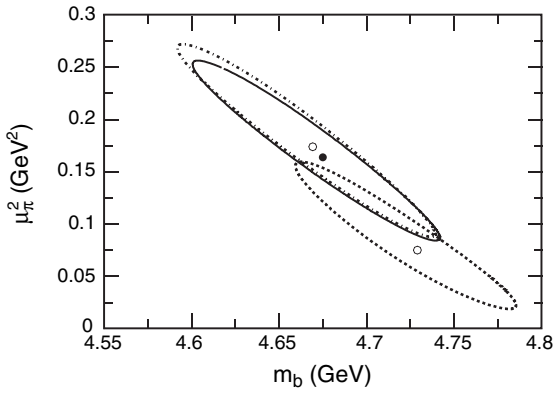


FIG. 6. Error ellipses corresponding to $\Delta\chi^2 = 1$ from the fit to the spectrum in the shape function scheme using the exponential (solid line), hyperbolic (dotted-dashed) and Gaussian (dashed line) models of the shape function. Both statistical and systematic errors have been taken into account.

## XII. MOMENTS OF THE PHOTON ENERGY SPECTRUM

The first moment is defined as the average of the photon energy spectrum, $\langle E_\gamma \rangle$, while higher moments are defined as $\langle (E_\gamma - \langle E_\gamma \rangle)^N \rangle$, where $N$ is the order of the moment under investigation. The values of the moments depend on the range of the photon energy spectrum used to calculate them. We vary the range by considering five different minimum photon energies $E_\gamma^{\rm min} = 1.897$, 1.999, 2.094, 2.181, and 2.261 GeV. These values correspond to the boundaries of the highest bins in hadronic mass, $M(X_s) =$ 2.8, 2.6, 2.4, 2.2, and 2.0 GeV.

The results for the first, second, and third moments of our photon energy spectrum as a function of the minimum photon energy are shown in Table VII. The third moments can be used to test the predictions for the $B \to X_s\gamma$ decay spectrum by dressed gluon exponentiation [41], but for now they are statistically limited. Figure 7 shows the first and second moments as a function of the minimum photon energy, together with the predictions from Ref. [20], which uses the parameters $m_b = 4.61$ GeV and $\mu_\pi^2 = 0.45$ GeV$^2$ that are obtained from fits to the $b \to c\ell\nu$ moments [21]. The solid lines represent the band allowed by theoretical uncertainties [40]. While the experimental errors decrease rapidly as the minimum photon energy is raised, the theoretical errors increase due to the ''bias'' corrections described in Ref. [20]. The agreement between the $b \to s\gamma$ and $b \to c\ell\nu$ moments is good, and well within the expected theoretical uncertainties. This demonstrates a nontrivial consistency between two different classes of inclusive $b$ decays.

We perform fits to the first and second moments to obtain values of the heavy-quark parameters which are less dependent on the details of the spectral shape. We take into account the correlation coefficients between the errors on the moments. The full correlation matrices are given in the appendix.

TABLE VII. First, second and third moments of the photon energy spectrum as a function of the minimum photon energy with statistical and systematic errors.

| $E_\gamma^{\rm min}$ (GeV) | $\langle E_\gamma \rangle$ (GeV) |
|---|---|
| 1.897 | $2.321 \pm 0.038^{+0.017}_{-0.038}$ |
| 1.999 | $2.314 \pm 0.023^{+0.014}_{-0.029}$ |
| 2.094 | $2.357 \pm 0.017^{+0.007}_{-0.017}$ |
| 2.181 | $2.396 \pm 0.013^{+0.003}_{-0.009}$ |
| 2.261 | $2.425 \pm 0.009^{+0.002}_{-0.004}$ |
| $E_\gamma^{\rm min}$ (GeV) | $\langle (E_\gamma - \langle E_\gamma \rangle)^2 \rangle$ (GeV$^2$) |
| 1.897 | $0.0253 \pm 0.0101^{+0.0041}_{-0.0028}$ |
| 1.999 | $0.0273 \pm 0.0037^{+0.0015}_{-0.0015}$ |
| 2.094 | $0.0183 \pm 0.0023^{+0.0010}_{-0.0007}$ |
| 2.181 | $0.0115 \pm 0.0014^{+0.0005}_{-0.0003}$ |
| 2.261 | $0.0075 \pm 0.0007^{+0.0002}_{-0.0002}$ |
| $E_\gamma^{\rm min}$ (GeV) | $\langle (E_\gamma - \langle E_\gamma \rangle)^3 \rangle$ (GeV$^3$) |
| 1.897 | $-0.0006 \pm 0.0012^{+0.0009}_{-0.0002}$ |
| 1.999 | $-0.0009 \pm 0.0006^{+0.0010}_{-0.0004}$ |
| 2.094 | $-0.0005 \pm 0.0003^{+0.0004}_{-0.0001}$ |
| 2.181 | $-0.0001 \pm 0.0001^{+0.0001}_{-0.0000}$ |
| 2.261 | $+0.0001 \pm 0.0001^{+0.0000}_{-0.0000}$ |

Using the shape function scheme, but ignoring theoretical uncertainties, we fit to the first and second moments at the lowest minimum photon energy $E_\gamma^{\rm min} = 1.897$ GeV. The fitted values are $m_b = (4.60^{+0.12}_{-0.14})$ GeV and $\mu_\pi^2 = (0.19^{+0.22}_{-0.20})$ GeV$^2$. These are in agreement with the fit to the full spectral shape, but have larger errors. A fit to the moments at the higher photon energy $E_\gamma^{\rm min} = 2.094$ GeV gives $m_b = (4.53^{+0.11}_{-0.14})$ GeV and $\mu_\pi^2 = (0.35^{+0.13}_{-0.14})$ GeV$^2$, and a fit to the highest photon energy $E_\gamma^{\rm min} = 2.261$ GeV reproduces the results from the fit to the spectrum.

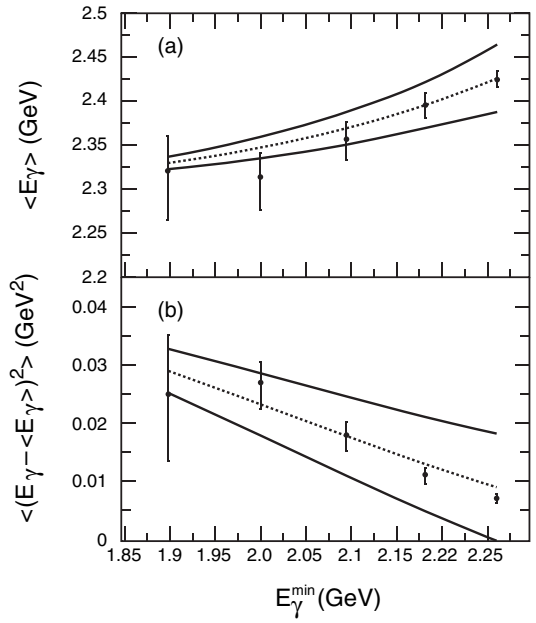


FIG. 7. First (a), and second (b) moments as a function of the minimum photon energy. The dotted lines show the predicted central values based on fits to the $b \to c\ell\nu$ moments [21], and the solid lines the theoretical uncertainties from the kinetic scheme [20,40].

Results with similar precision are obtained from fits using the kinetic scheme if theoretical uncertainties are ignored. At the higher photon energies the theoretical predictions for inclusive quantities such as moments are not very reliable, as shown by the solid lines in Fig. 7. It appears that an optimal combination of experimental and theoretical uncertainties occurs in the range $E_\gamma^{\rm min} = 1.9$–$2.1$ GeV.

## XIII. CONCLUSIONS

We have measured the inclusive $b \to s\gamma$ branching fraction for $E_\gamma > 1.9$ GeV and extrapolated it to $E_\gamma > 1.6$ GeV. Our result is in good agreement with the world average. Although our measurement is currently systematics limited, with more data we expect to improve our understanding of the missing fraction of high multiplicity $X_s$ hadronic final states, and therefore reduce our dominant systematic error. We have made the first measurement of the isospin asymmetry between $B^- \to X_{s\bar{u}}\gamma$ and $\overline{B}^0 \to X_{s\bar{d}}\gamma$, and found that it is consistent with zero within the experimental uncertainty, which is mainly statistical.

We have made a measurement of the $b \to s\gamma$ spectral shape over the range $E_\gamma > 1.9$ GeV. After taking into account the presence of the $K^*(892)$ resonance, the shape is found to agree well with two recent theoretical calculations. Fits to the spectrum are used to give values for the heavy-quark parameters $m_b$ and $\mu_\pi^2$ in the two schemes. We calculate the first, second, and third moments of the photon spectrum for five different minimum values of the photon energy between 1.90 and 2.26 GeV. The moments are in good agreement with predictions based on fits to the measured $b \to c\ell\nu$ moments. Fits to the photon energy moments give heavy-quark parameters which agree with the fits to the full spectrum, but are less accurate. Information from $b \to s\gamma$ and $b \to c\ell\nu$ can be combined to obtain tighter constraints on $m_b$ and $\mu_\pi^2$. This will lead to improved extractions of $|V_{ub}|$ from the measurements of $b \to u\ell\nu$ decays.

While this paper was in preparation, new references appeared concerning both the photon energy spectrum and the moments. Reference [41] computes the photon energy spectrum and moments by resummed perturbation theory, using the technique of dressed gluon exponentiation. The predicted spectrum extends smoothly into the nonperturbative region and tends to zero at the physical end point. The predictions for the moments have been compared to our results and are consistent with them. Reference [42] presents fits to the BELLE spectrum [24] in the shape function scheme. Reference [43] shows predictions for the photon energy moments using an OPE

approach calculated to NNLO accuracy. This does not require spectral information from the shape functions. These predictions are fit to the experimental moments from the BELLE spectrum and to the moments from this analysis. The new preprints indicate the current interest in the extraction of heavy-quark parameters from the shape of the $b \to s\gamma$ spectrum, and show how our data will contribute to improved knowledge of these parameters.

## ACKNOWLEDGMENTS

We have greatly benefited from many discussions with D. Benson, I. I. Bigi, A. L. Kagan, M. Neubert, and N. Uraltsev. In particular, we would like to thank A. L. Kagan for providing us with a computer code implementing the calculations in Ref. [9], M. Neubert for making available for us a program with the shape function scheme calculations and D. Benson for providing us with tabulated values of the photon energy spectrum in the kinetic scheme. We are grateful for the extraordinary contributions of our PEP-II colleagues in achieving the excellent luminosity and machine conditions that have made this work possible. The success of this project also relies critically on the expertise and dedication of the computing organizations that support *BABAR*. The collaborating institutions wish to thank SLAC for its support and the kind hospitality extended to them. This work is supported by the U.S. Department of Energy and National Science Foundation, the Natural Sciences and Engineering Research Council (Canada), Institute of High Energy Physics (China), the Commissariat à l'Energie Atomique and Institut National de Physique Nucléaire et de Physique des Particules (France), the Bundesministerium für Bildung und Forschung and Deutsche Forschungsgemeinschaft (Germany), the Istituto Nazionale di Fisica Nucleare (Italy), the Foundation for Fundamental Research on Matter (The Netherlands), the Research Council of Norway, the Ministry of Science and Technology of the Russian Federation, and the Particle Physics and Astronomy Research Council (United Kingdom). Individuals have received support from CONACyT (Mexico), the A. P. Sloan Foundation, the Research Corporation, and the Alexander von Humboldt Foundation.

## APPENDIX

In this appendix we present more detailed information concerning the fit to the spectrum and the correlation matrices for the moments.

### 1. Ellipse from the fit to the spectrum for the shape function scheme

Table VIII lists the points on the ellipse from the fit to the spectrum using the exponential model in the shape function scheme and shown in Fig. 6.

TABLE VIII. Heavy-quark parameters, $m_b$ and $\mu_\pi^2$, evaluated along the $\Delta\chi^2 = 1$ contour resulting from the fit to the spectrum using the shape function scheme.

| $m_b$(GeV) | $\mu_\pi^2$(GeV$^2$) | $m_b$(GeV) | $\mu_\pi^2$(GeV$^2$) |
|---|---|---|---|
| 4.618 | 0.249 | 4.730 | 0.088 |
| 4.629 | 0.240 | 4.721 | 0.095 |
| 4.636 | 0.233 | 4.716 | 0.099 |
| 4.642 | 0.227 | 4.709 | 0.106 |
| 4.647 | 0.222 | 4.702 | 0.112 |
| 4.655 | 0.213 | 4.697 | 0.118 |
| 4.662 | 0.205 | 4.692 | 0.124 |
| 4.669 | 0.197 | 4.686 | 0.129 |
| 4.675 | 0.190 | 4.681 | 0.135 |
| 4.680 | 0.183 | 4.677 | 0.140 |
| 4.685 | 0.177 | 4.672 | 0.146 |
| 4.690 | 0.171 | 4.667 | 0.152 |
| 4.694 | 0.165 | 4.659 | 0.162 |
| 4.702 | 0.154 | 4.650 | 0.173 |
| 4.709 | 0.145 | 4.642 | 0.183 |
| 4.715 | 0.136 | 4.634 | 0.194 |
| 4.721 | 0.127 | 4.627 | 0.204 |
| 4.726 | 0.120 | 4.620 | 0.214 |
| 4.730 | 0.113 | 4.614 | 0.224 |
| 4.734 | 0.106 | 4.608 | 0.233 |
| 4.737 | 0.100 | 4.604 | 0.241 |
| 4.739 | 0.095 | 4.601 | 0.249 |
| 4.741 | 0.090 | 4.601 | 0.255 |
| 4.742 | 0.087 | 4.603 | 0.257 |
| 4.740 | 0.084 | 4.607 | 0.257 |

### 2. Correlation matrices for the moments

Here we present the correlation matrices for the first and second moments. Table IX shows the statistical correlation matrix and Table X shows the systematic correlation matrix.

TABLE IX. Statistical correlation coefficients for the moments with different minimum cuts on the photon energy.

| | $E^{\rm min}$(GeV) | 1.897 | 1.999 | 2.094 | 2.181 | 2.261 |
|---|---|---|---|---|---|---|
| | | | $\langle E\rangle$ | | | |
| | 1.897 | 1 | 0.55 | 0.28 | 0.12 | 0.033 |
| | 1.999 | | 1 | 0.47 | 0.19 | 0.046 |
| $\langle E\rangle$ | 2.094 | | | 1 | 0.48 | 0.18 |
| | 2.181 | | | | 1 | 0.45 |
| | 2.261 | | | | | 1 |
| | | | | $\langle (E-\langle E\rangle)^2\rangle$ | | |
| | 1.897 | 1 | 0.28 | 0.03 | −0.07 | -0.06 |
| | 1.999 | | 1 | 0.16 | −0.14 | −0.14 |
| $\langle (E-\langle E\rangle)^2\rangle$ | 2.094 | | | 1 | 0.13 | −0.09 |
| | 2.181 | | | | 1 | 0.17 |
| | 2.261 | | | | | 1 |
| | | | | $\langle (E-\langle E\rangle)^2\rangle$ | | |
| | 1.897 | −0.90 | −0.41 | −0.23 | −0.12 | −0.05 |
| | 1.999 | | −0.79 | −0.40 | −0.19 | −0.08 |
| $\langle E\rangle$ | 2.094 | | | −0.79 | −0.42 | −0.18 |
| | 2.181 | | | | −0.82 | −0.37 |
| | 2.261 | | | | | −0.76 |

TABLE X. Systematic correlation coefficients for the moments with different minimum cuts on the photon energy.

| | $E^{\min}$ (GeV) | 1.897 | 1.999 | 2.094 | 2.181 | 2.261 |
|---|---|---|---|---|---|---|
| | | | | $\langle E \rangle$ | | |
| | 1.897 | 1 | 0.98 | 0.97 | 0.93 | 0.85 |
| | 1.999 | | 1 | 0.98 | 0.95 | 0.84 |
| $\langle E \rangle$ | 2.094 | | | 1 | 0.97 | 0.86 |
| | 2.181 | | | | 1 | 0.92 |
| | 2.261 | | | | | 1 |
| | | | | $\langle (E - \langle E \rangle)^2 \rangle$ | | |
| | 1.897 | 1 | 0.87 | 0.86 | 0.62 | 0.30 |
| | 1.999 | | 1 | 0.90 | 0.70 | 0.27 |
| $\langle (E - \langle E \rangle)^2 \rangle$ | 2.094 | | | 1 | 0.85 | 0.38 |
| | 2.181 | | | | 1 | 0.67 |
| | 2.261 | | | | | 1 |
| | | | | $\langle (E - \langle E \rangle)^2 \rangle$ | | |
| | 1.897 | −0.93 | −0.87 | −0.91 | −0.71 | −0.26 |
| | 1.999 | | −0.90 | −0.91 | −0.74 | −0.22 |
| $\langle E \rangle$ | 2.094 | | | −0.90 | −0.75 | −0.21 |
| | 2.181 | | | | −0.73 | −0.20 |
| | 2.261 | | | | | −0.08 |


[1] P. Gambino and M. Misiak, Nucl. Phys. **B611**, 338 (2001).
[2] A. J. Buras, A. Czarnecki, M. Misiak, and J. Urban, Nucl. Phys. **B631**, 219 (2002).
[3] M. Neubert, Eur. Phys. J. C **40**, 165 (2005).
[4] J. Alexander *et al.* (Heavy Flavor Averaging Group), hep-ex/0412073.
[5] K. Bieri, C. Greub, and M. Steinhauser, Phys. Rev. D **67**, 114019 (2003); P. Gambino, M. Gorbahn, and U. Haisch, Nucl. Phys. **B673**, 238 (2003); M. Misiak and M. Steinhauser, Nucl. Phys. **B683**, 277 (2004); I. Blokland, A. Czarnecki, M. Misiak, M. Slusarczyk and F. Tkachov, Phys. Rev. D **72**, 033014 (2005); M. Gorbahn and U. Haisch, Nucl. Phys. **B713**, 291 (2005); M. Gorbahn, U. Haisch, and M. Misiak, hep-ph/0504194; H. M. Asatrian, C. Greub, A. Hovhannisyan, T. Hurth, and V. Poghosyan, Phys. Lett. B **619**, 322 (2005).
[6] B. Grinstein and M. B. Wise, Phys. Lett. B **201**, 274 (1988).
[7] W. S. Hou and R. S. Willey, Phys. Lett. B **202**, 591 (1988).
[8] J. L. Hewett and J. D. Wells, Phys. Rev. D **55**, 5549 (1997).
[9] A. L. Kagan and M. Neubert, Eur. Phys. J. C **7**, 5 (1999).
[10] T. Hurth, Rev. Mod. Phys. **75**, 1159 (2003).
[11] M. Neubert, Phys. Rev. D **49**, 4623 (1994).
[12] I. I. Bigi and N. Uraltsev, Int. J. Mod. Phys. A **17**, 4709 (2002).
[13] I. I. Bigi and N. Uraltsev, Phys. Lett. B **579**, 340 (2004).
[14] C. W. Bauer and A. V. Manohar, Phys. Rev. D **70**, 034024 (2004).
[15] S. W. Bosch, B. O. Lange, M. Neubert, and G. Paz, Nucl. Phys. **B699**, 335 (2004).
[16] S. W. Bosch, M. Neubert, and G. Paz, J. High Energy Phys. 11 (2004) 073.
[17] B. O. Lange, M. Neubert, and G. Paz, hep-ph/0504071 [Phys. Rev. D (to be published)].
[18] M. Neubert, hep-ph/0411027 [Eur. Phys. J. C (to be published)].
[19] M. Neubert, Phys. Lett. B **612**, 13 (2005).
[20] D. Benson, I. I. Bigi, and N. Uraltsev, Nucl. Phys. **B710**, 371 (2005).
[21] B. Aubert *et al.* (*BABAR* Collaboration), Phys. Rev. Lett. **93**, 011803 (2004).
[22] M. S. Alam *et al.* (CLEO Collaboration), Phys. Rev. Lett. **74**, 2885 (1995); T. E. Coan *et al.* (CLEO Collaboration), Phys. Rev. Lett. **86**, 5661 (2001); S. Chen *et al.* (CLEO Collaboration), Phys. Rev. Lett. **87**, 251807 (2001).
[23] R. Barate *et al.* (ALEPH Collaboration), Phys. Lett. B **429**, 169 (1998).
[24] P. Koppenburg *et al.* (BELLE Collaboration), Phys. Rev. Lett. **93**, 061803 (2004).
[25] K. Abe *et al.* (BELLE Collaboration), Phys. Lett. B **511**, 151 (2001); S. Nishida *et al.* (BELLE Collaboration), Phys. Rev. Lett. **93**, 031803 (2004).
[26] B. Aubert *et al.* (*BABAR* Collaboration), Phys. Rev. Lett. **93**, 021804 (2004).
[27] B. Aubert *et al.* (*BABAR* Collaboration), Nucl. Instrum. Methods Phys. Res., Sect. A **479**, 1 (2002).
[28] M. Nakao *et al.* (BELLE Collaboration), Phys. Rev. D **69**, 112001 (2004); B. Aubert *et al.* (*BABAR* Collaboration), Phys. Rev. D **70**, 112006 (2004).
[29] S. Nishida *et al.* (BELLE Collaboration), Phys. Rev. Lett. **89**, 231801 (2002); K. Abe *et al.* (BELLE Collaboration), hep-ex/0408138.
[30] S. Veseli and M. G. Olsson, Phys. Lett. B **367**, 309 (1996); D. Ebert, R. N. Faustov, V. O. Galkin, and H. Toki, Phys. Rev. D **64**, 054001 (2001); A. Safir, Eur. Phys. J. direct C

**3**, 1 (2001); H. Y. Cheng and C. K. Chua, Phys. Rev. D **69**, 094007 (2004).

[31] Torbjörn Sjöstrand, ''PYTHIA 5.7 and JETSET 7.4: Physics and Manual'' (Lund University), hep-ph/9508391; T. Sjöstrand, Comput. Phys. Commun. **82**, 74 (1994).

[32] S. Agostinelli *et al.*, Nucl. Instrum. Methods Phys. Res., Sect. A **506**, 250 (2003).

[33] S. Eidelman *et al.* (Particle Data Group), Phys. Lett. B **592**, 1 (2004).

[34] G. C. Fox and S. Wolfram, Nucl. Phys. **B149**, 413 (1979).

[35] T. Skwarnicki, DESY internal report DESY-F31-86-02 (1986).

[36] The Novosibirsk function is defined as $f(m_{\rm ES}) = A_S \exp(-0.5\{\ln^2[1 + \Lambda\tau \cdot (m_{\rm ES} - m_0)]/\tau^2 + \tau^2\})$, where $\Lambda = \sinh(\tau\sqrt{\ln 4})/(\sigma\tau\sqrt{\ln 4})$, the peak position is $m_0$, the width is $\sigma$, and $\tau$ is the tail parameter.

[37] H. Albrecht *et al.* (ARGUS Collaboration), Z. Phys. C **48**, 543 (1990).

[38] A. L. Kagan and M. Neubert, Phys. Lett. B **539**, 227 (2002).

[39] B. Aubert *et al.* (*BABAR* Collaboration), Phys. Rev. D **69**, 071101 (2004).

[40] D. Benson, I. I. Bigi, and N. Uraltsev (private communication).

[41] E. Gardi and J. R. Andersen, hep-ph/0504140; E. Gardi, J. High Energy Phys. 04 (2004) 049; J. R. Andersen and E. Gardi, hep-ph/0502159.

[42] I. Bizjak, A. Limosani, and T. Nozaki, hep-ex/0506057.

[43] M. Neubert, hep-ph/0506245 [Phys. Rev. D (to be published)].